

Verso: Front. Struct. Civ. Eng. 2025

Recto: Sina SARFARAZI et al. Stainless-steel Connections: An XML Framework

Front. Struct. Civ. Eng. 2025

RESEARCH ARTICLE

<https://doi.org/10.1007/s11709-025-1162-y>

Exploring the stainless-steel beam-to-column connections response: A hybrid explainable machine learning framework for characterization

Sina SARFARAZI^{a*}, Rabee SHAMASS^b, Federico GUARRACINO^a, Ida MASCOLO^a, Mariano MODANO^a

^a Department of Structures for Engineering and Architecture, University of Naples “Federico II,” Naples 80125, Italy

^b Department of Civil and Environmental Engineering, Brunel University London, London, UB8 3PH, UK

*Corresponding author. E-mail: sina.srfz@gmail.com

ABSTRACT Stainless-steel provides substantial advantages for structural uses, though its upfront cost is notably high. Consequently, it's vital to establish safe and economically viable design practices that enhance material utilization. Such development relies on a thorough understanding of the mechanical properties of structural components, particularly connections. This research advances the field by investigating the behavior of stainless-steel connections through the use of a four-parameter fitting technique and explainable artificial intelligence methods. Training was conducted on eight different machine learning algorithms—namely, Decision Tree, Random Forest, K-Nearest Neighbors, Gradient Boosting, Extreme Gradient Boosting, Light Gradient Boosting, Adaptive Boosting, and Categorical Boosting. SHapley Additive Explanations was applied to interpret model predictions, highlighting features like spacing between bolts in tension and end-plate height as highly impactful on the initial rotational stiffness and plastic moment resistance. Results showed that Extreme Gradient Boosting achieved a coefficient of determination score of 0.99 for initial stiffness and plastic moment resistance, while Gradient Boosting model had similar performance with maximum moment resistance and ultimate rotation. A user-friendly graphical user interface (GUI) was also developed, allowing engineers to input parameters and get rapid moment–rotation predictions. This framework offers a data-driven, interpretable alternative to conventional methods, supporting future design recommendations for stainless-steel beam-to-column connections.

KEYWORDS steel connections, stainless-steel, machine learning, explainable models, moment–rotation response

1 Introduction

Flush end-plate connections (FECs) have a wide application in the construction industry because of their good flexural resistance and economic efficiencies during fabrication and installation [1]. This type of connection is used in frames with moderately short beams and exposed to standard static loads with relatively small lateral loads [1,2]. FECs are considered a viable alternative to beam-to-column joints in moment-resisting frames [3].

Stainless-steel, a class of corrosion-resistant alloys of iron, is a recent new structural steel with superior mechanical characteristics, higher tensile strength, toughness, high temperature and corrosion resistances, low cost of maintenance, and a more pleasing appearance than conventional carbon steel [4]. Because of its durability, recyclability, and corrosion resistance, no toxic protection coatings are needed, making it an eco-friendly construction material [5]. Furthermore, by replacing carbon steel with stainless-steel, the dimensions of the structural members may be reduced considerably, providing significant financial benefits, like reduced welding, logistics, and installation costs [6]. However, the adequacy of the existing theoretical design procedures for stainless-steel connections is limited. For example, Kim and Kuwamura [7] presented the finite element (FE) modeling of bolted joints in thin-walled stainless-steel plates subjected to static shear loads. Bouchair et al. [8] investigated two types of bolted joints, including cover plate connections and T-stubs, in which the bolts were subjected to shear or tension loading. Salih et al. [9] conducted experimental tests and numerical analysis on the bearing failure of stainless-steel bolted joints subjected to static shear loading. Yuan

et al. [10] performed analytical and test investigations on T-stubs in tension to formulate plastic moment parameters. Gao et al. [11] investigated experimentally and numerically the behavior of stainless-steel double extended end-plate beam-to-column joints under monotonic loading. Kong et al. [12] proposed mathematical expressions for predicting the stiffness and maximum moment of stainless-steel web cleat connections. Elflah et al. [13] conducted experimental and numerical investigations on different stainless-steel joint configurations. Hasan et al. [14] proposed a simple analytical model to predict the moment–rotation behavior of austenitic stainless-steel top and seat angle cleat connections subjected to monotonic loading. Eladly and Schafer [15] proposed a simple model for predicting the moment–rotation response of austenitic stainless-steel extended end-plate connections subjected to monotonic loading. Song et al. [16] investigated numerically and experimentally ultimate moment and rotational capacity of stainless-steel end-plate connections.

Assessing the moment–rotation (M – Φ) characteristics of joints is essential in steel design, with experimental testing historically acting as the preferred method due to its direct observation of actual performance. However, these tests are often very expensive. Because of this, other methods like analytical, empirical, mechanical, and numerical simulation have been developed to make the design process easier. In the analytical method, mathematical equations are used to predict joint behavior, which makes it accurate and fast under certain conditions. But this method is less effective for larger deformations or complex forces. The empirical method is another option, where predictions are based on curves fitted from existing data. This method is easier to use for engineers who may not have many computation resources, but it can be less reliable, especially for complex joints. The component method breaks down a connection into parts like bolts and plates, giving a very detailed view of how each part behaves. However, it requires a lot of data for each piece, which can make it more complicated. Further advancements in Finite Element Analysis (FEA) have shown its adaptability in addressing complex structural behaviors and nonlinear challenges [17–19]. Despite its strengths, FEA requires strong computing power and skilled users, which makes it challenging for those with limited resources. On the other hand, over the past few years, significant progress has been made in applying Machine Learning (ML) methodologies to various engineering problems, especially in structural and material modeling. ML approaches have been found promising for predicting complex material behavior, enabling the modeling of complex interactions and providing alternatives to computationally demanding traditional methods. For example, adaptive collocation techniques and deep learning models for solving partial differential equations illustrate innovative uses of ML in computational mechanics [20,21]. Meanwhile, Advanced ML applications for complex materials have been explored in recent studies. For example, in work by Liu et al. [22], particle swarm optimization was combined with artificial neural networks (ANNs) to improve prediction accuracy for polymer nanocomposites. Liu et al. [23] used a stochastic multi-scale ML framework with FE modeling to predict thermal conductivity in graphene-enhanced composites, with SHapley Additive Explanations (SHAP) applied to enhance model transparency and interpretability. Other studies have demonstrated various advanced ML applications in material modeling, such as the use of hybrid methods for predicting pipeline material strength, and the use of surrogate models and multiscale approaches for managing complex material behaviors [24–28]. This progress has led to a growing interest in using ML to address issues specific to structural engineering, such as beam-to-column connections. For example, Gao and Lin [29] predicted failure mode of reinforced concrete (RC) interior beam-column joints utilizing 580 experimental results. Mangalathu and Jeon [30] presented the classification of failure mode and the prediction of associated shear strength of RC beam-column joints using 536 experimental test data. Alwanas et al. [31] implemented an extreme ML method for forecasting the load-carrying capacity and failure mode of RC joints. Park et al. [32] suggested a prediction model of uniaxial shear strength under uniaxial cyclic loading using artificial neural network (ANN), and gene expression programming for exterior RC beam-column joints. Kotsovou et al. [33] presented a prediction ANN model considering failure mode and strength assessment of RC exterior beam-column joints. Haido [34] introduced novel ANN models to evaluate the shear strength and failure mode of RC exterior and interior beam-column joints. Alagundi and Palanisamy [35] proposed an ANN model to predict the RC exterior beam-column joint shear strength. Naderpour and Nagai [36] developed innovative predictive models for shear capacity of RC exterior joints using multiple soft computing approaches. Shah et al. [37] implemented ANNs, adaptive neuro fuzzy inference system, and linear genetic programming, to predict the moment–rotation response of boltless carbon steel connections. Cao et al. [38] developed the extreme ML method to predict the moment capacity of beam to column carbon steel connections. Abdalla and Stavroulakis [39] proposed a backpropagation neural network model for analyzing semi-rigid carbon steel connections.

Faridmehr et al. [40] evaluated the joint initial stiffness ($S_{j,ini}$) and ultimate moment capacity (M_u) of top-seat angle carbon steel connections with double web angles using ANN model. Kueh [41] suggested a mathematical moment–rotation formula using ANN and multilinear regression approaches for predicting moment–rotation response of FEP carbon steel beam-to-column connections. Sarothi et al. [42] studied the application of ML for predicting the bearing strength of double shear bolted connections in structural steel. Anderson et al. [43] implemented an ANN model to explore the response of minor-axis connections. Tran and Kim [44] using novel hybrid models, predicted the moment–rotation response of carbon steel flush endplate joints, specifically ANN integrated with hunter-prey optimization. Lima et al. [45] developed ANN model to estimate the moment resistance and initial stiffness of beam-to-column carbon steel joints.

This study, first, proposes a novel methodology which is suitable for characterizing the entire moment–rotation response of steel beam to column connections, including their ultimate moment and rotation capacity. This is achieved by integrating a four-parameter bilinear approach to ML techniques. As shown in Section 2, this method uses four parameters: the initial rotational stiffness ($S_{j,ini}$), plastic moment resistance ($M_{j,R}$), the maximum moment ($M_{j,max}$), and the ultimate rotation ($\Phi_{j,u}$). By generating a large data set and training an appropriate ML algorithm, these parameters can be accurately derived, enabling the prediction of the entire moment–rotation response of the connections. This methodology is general and can be applicable in any steel beam-to-column connection, regardless of connection types and materials. To the best of the authors’ knowledge, there is no literature available that examines the behavior of stainless-steel beam-to-column FECs; hence, the proposed general methodology is implemented, to investigate the response of this type of connections. In this regard, based on an extensive list of stainless-steel sections provided by the British Stainless-steel Association [46], and using a Python scripting interface [47], a comprehensive database is generated considering extracting moment–rotation data from 612 FE samples. Subsequently, eight widely recognized ML models including: Decision Tree (DT), Random Forest (RF), K-Nearest Neighbors (KNN), Gradient Boosting (GB), Extreme Gradient Boosting (XGB), Light Gradient Boosting Machine (LGBM), Adaptive Boosting (AdaBoost) and Categorical Boosting (CatBoost) are employed to train and evaluate the system. The best predictive model is then selected for each output target to proceed with the next part of the research, which is focused on ML interpretability.

Second, this research advances the transparency and interpretability of ML applications in the investigated field by using the explainable machine learning (EML) approach. This is achieved using the SHAP algorithm, which provides explanations for ML predictions. The considered approach not only predicts the entire moment–rotation response but also clarifies the factors influencing it. Previous studies using ML to predict the response of carbon steel, concrete or composite connections have mainly focused on predicting resistance, which establishes black box solutions that do not explain the physics of the problem. This opacity is a major criticism of existing ML methodologies. By using EML techniques, this study aims to provide further clarifications into the mechanics of beam-to-column connection, thus addressing the interpretability limitation in current ML application. In summary, the contributions of this study are as follows.

- 1) Proposing a four-parameter bilinear model integrated with ML techniques to characterize the complete moment–rotation ($M-\Phi$) response of stainless-steel beam-to-column connections.
- 2) Investigating the ($M-\Phi$) response of stainless-steel FECs using the proposed methodology.
- 3) Presenting a comprehensive application of the EML approach with the SHAP algorithm, which enhances transparency and understanding of model functionality through both global explanations (for overall model behavior) and local explanations (for individual predictions).
- 4) Developing a graphical user interface (GUI) that enables users to predict and plot the ($M-\Phi$) response, thereby making the models more accessible and user-friendly for structural engineers.

A brief overview of the study’s methodology is provided in Fig. 1.

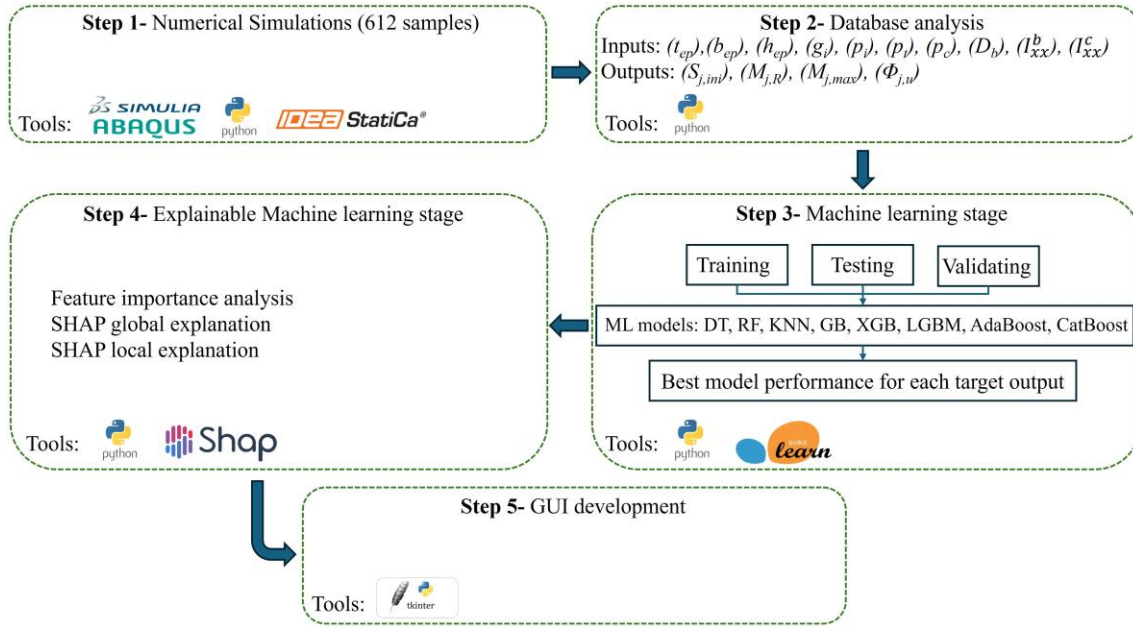


Fig. 1 Methodological process and research steps.

2 Moment rotation behavior of the connections

The plotting of the connection's moment–rotation curve is an essential tool for understanding how the connection responds to various loading situations. Three primary aspects are revealed by the curve: stiffness, resistance, and rotational capacity. The stiffness of a connection can be categorized into three distinct types by considering the slope of the ($M-\Phi$) curve at specific rotations: the initial stiffness ($S_{j,ini}$), the secant stiffness (S_j), and the tangent stiffness ($S_{j,pp}$). Furthermore, the ($M-\Phi$) curves provide essential information, including, maximum moment ($M_{j,max}$), the plastic moment resistance ($M_{j,R}$), and the corresponding ultimate rotation ($\Phi_{j,u}$) (see Fig. 2).

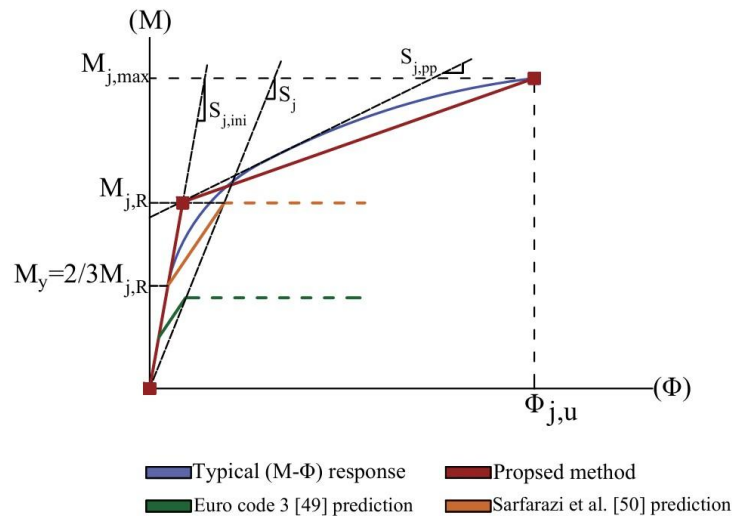


Fig. 2 Moment–rotation characteristics of stainless-steel connection.

In terms of the ductility and mechanical properties of stainless-steel, it appears that these aspects have been somewhat neglected in the development of current calculation methods and design standards, which were initially formulated for carbon steel. Sarfarazi et al. [48] examined design approaches for stainless-steel beam-

to-column connections and indicated that the experimental results of stainless-steel joints are not align with the predictions made by the Eurocode 3 (EC3) component method [49], which relies on the material proof strength ($f_{0.2}$) concept. Particularly EC3 rules [49] seem to underestimate the plastic moment resistance. Additionally, EC3 [49] does not explicitly consider the pronounced nonlinear stress-strain properties with considerable strain hardening provided by stainless-steel. It's important to acknowledge that EC3 [49] lacks a definitive formula for calculating the rotational capacity of steel connections. This rotational capacity is defined as the degree to which a joint can pivot while maintaining its strength at a pseudo-plastic state. To obtain better predictions of plastic resistance ($M_{j,R}$), Sarfarazi et al. [50] proposed an equivalent yield strength ($f_{y,equivalent}$) instead of material proof strength ($f_{0.2}$). Based on these findings, it has been shown that using established carbon steel procedures with a specially adapted material, developed using the secant stiffness method, aligns the results with those of experimentally validated numerical simulations. By utilizing this procedure, their proposed method could provide insights into the potential advantages of using stainless-steel in engineering design. In spite of this, given its development based on the EC3 [49] methodology, there is still a need for an approach that can replicate the full moment-rotation response of stainless-steel beams. In this work, a four-parameter fitting approach for characterizing the entire moment-rotation response of stainless-steel FECs is presented. The four parameters are: the initial rotational stiffness ($S_{j,ini}$), plastic moment resistance ($M_{j,R}$), the maximum moment ($M_{j,max}$), and the ultimate rotation ($\Phi_{j,u}$) (see Fig. 2). To identify stiffness, a straight line from the zero-loading point to the joint's elastic moment (typically set at $M_y = 2/3 M_{j,R}$) can be adjusted. The plastic moment resistance ($M_{j,R}$) can be derived from experimental or FE moment-rotation curves. This involves utilizing the intersection of two linear sections of the moment-rotation curve (lines slope are: $S_{j,ini}$ and $S_{j,pp}$), which is depicted in Fig. 2. The maximum moment ($M_{j,max}$), and the corresponding ultimate rotation ($\Phi_{j,u}$) are also the last data points prior to failure of the connection.

Having these four parameters allows for the complete characterization of the curve. To obtain and predict these parameters, a large database must be prepared and ML algorithms applied. Once these parameters are determined, the response of connections can be derived using the defined bilinear curve.

3 Adapted finite element technique for data generation

3.1 Development of finite element model

The current authors have already proposed [48,50] a 3D nonlinear FE model using ABAQUS [47] to simulate the complex interaction between bolted connection components. Building on this FE model, a numerical modeling procedure of FECs is presented and validated in this paper. The validated numerical model is utilized then by ABAQUS scripting interface with Python [47] to create loops and automatically regenerate the samples and data set. The nonlinear relationship proposed by Rasmussen [51] was employed to model the stainless-steel material behavior. The mechanical characteristics of austenitic stainless-steel material, were determined following the guidelines outlined in EC3, Part 1-4 (EN 1993-1-4) [49]. A model summary is given by Eq. (1) to (6), where E_0 is the material Young's modulus, σ and ε are stress and strain, $\sigma_{0.2}$ is the 0.2% proof stress and n and m are strain hardening exponents. Calibration of the nonlinear variables was carried out as suggested in Ref. [47].

$$\varepsilon = \begin{cases} \frac{\sigma}{E_0} + 0.002 \left(\frac{\sigma}{\sigma_{0.2}} \right)^n & \sigma \leq \sigma_{0.2} \\ \varepsilon_{0.2} + \frac{\sigma - \sigma_{0.2}}{E_{0.2}} + \varepsilon_u \left(\frac{\sigma - \sigma_{0.2}}{\sigma_u - \sigma_{0.2}} \right)^m & \sigma > \sigma_{0.2} \end{cases}, \quad (1)$$

$$n = \frac{\ln(20)}{\ln\left(\frac{\sigma_{0.2}}{\sigma_{0.01}}\right)}, \quad (2)$$

$$m = 1 + 3.5 \frac{\sigma_{0.2}}{\sigma_u}, \quad (3)$$

$$E_{0.2} = \frac{E_0}{1 + 0.002n \frac{E_0}{\sigma_{0.2}}}, \quad (4)$$

$$\varepsilon_u = 1 - \frac{\sigma_{0.2}}{\sigma_u}, \quad (5)$$

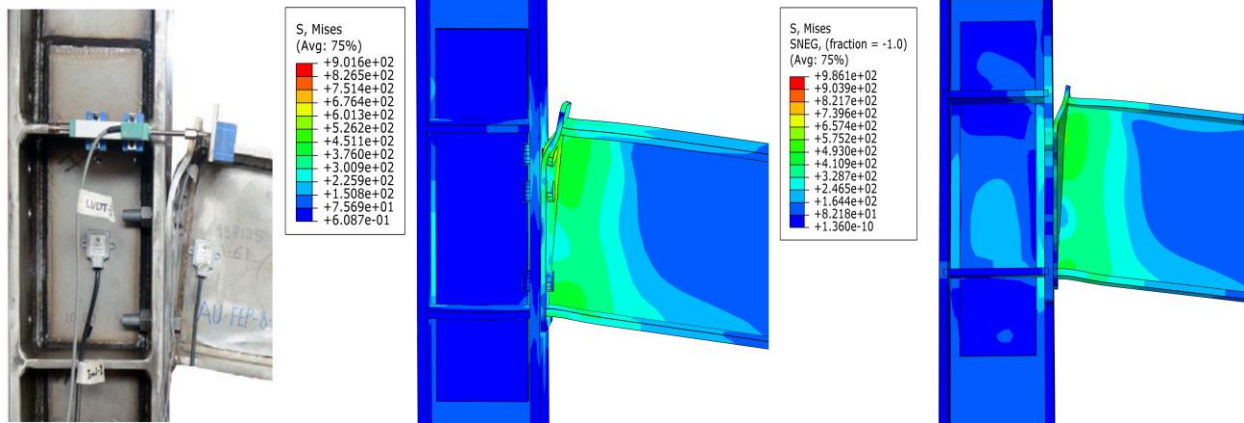
$$\frac{\sigma_{0.2}}{\sigma_u} = 0.2 + 185 \frac{\sigma_{0.2}}{E_0}, \quad (6)$$

For contact analysis, the “main-secondary” methodology from ABAQUS [47] was implemented. Finer mesh areas were considered secondary, while coarser were selected as the main surface. A small sliding surface-to-surface separation technique was employed for the contact relationships between the non-welded components of joints (e.g., between column flange and plate). The tangential behavior was considered for modeling the surface contact properties between the elements based on defining penalty friction with a friction coefficient value of 0.3. To facilitate full transferring of compressive loads and separation after contact, for all models, “hard contact” was assumed. In this study, to model the bolts, a simplified approach with the “Cartesian” connector element available in ABAQUS [47], which can be defined as spring with “elastic-plastic and failure” characteristics in the axial and shear directions, is employed. Implementing these elements is a computationally more efficient approach, instead of explicitly simulating the bolts using solid elements. Moreover, they offer excellent simulation accuracy [15,48,50,52]. Cartesian connector elements connect two individual bolt positions, where three local coordinate systems measure the change in translational degrees of freedom. Since the bolts do not constrain the rotation of connected parts, the rotational degrees of freedom are ignored. For the joints studied in this work, the translational axial behavior is defined for the y-direction of the connection. The radial shear behavior corresponding to the x and z directions can be assumed to be the same due to the axisymmetric characteristics of the joint. To avoid undesirable deformations appearing in the connector region, “rigid body” constraints [47] were implemented. A rigid body is known as a set of points in which the distance within points remains unchanged throughout the analysis. Therefore, the body does not deform or change shape but can exhibit large rigid body motions. The diameter of the rigid body is considered equal to the simulated standard bolt hole (e.g., for M16 bolt: equal to 18 mm). To model the specimens, quadrilateral four-node shell elements (S4R elements) were implemented. Considering the computing time and the very large number of parametric analyses required, the use of shell elements has proven much more efficient compared to solid elements. This type of element has been successfully applied to several analyses so far [48,53–55]. Following a mesh sensitivity analysis, a variety of mesh sizes (2–40 mm) were evaluated to determine the optimum mesh size for each part. Then a structured mesh with varying dimensions was considered. For regions exposed to concentrated stresses, a finer mesh size (5 mm) was adopted, while the rest of the model was simulated with a coarser size (20 mm).

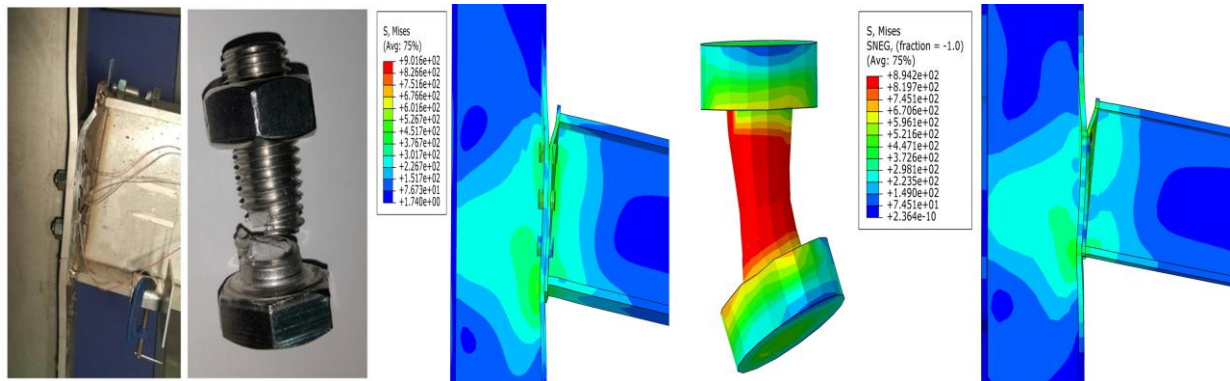
3.2 Numerical model validation

In this section, the FE modeling validation was carried out in line with the general framework in Section 3.1. Specifically, material properties, along with geometric details of the chosen specimens, were taken from comprehensive test reports [13,16]. The model’s efficacy in replicating the mechanical behavior of various connection types is assessed through a comparison with experimental results of four different stainless-steel connections tested by [13,16] and their 3D solid FE counterparts. The failure mechanism at the deformation associated with the highest load is depicted in Fig. 3. According to Fig. 3(a) and 3(b), the failure mode observed in the experimental data for flush end-plate (FEP) connection types was closely mirrored by both the 3D shell and 3D solid models, including large plastic deformations close to the experimental observations that were exhibited by the column flange and end-plate of the FE models. Additionally, the failure of the connectors corresponding to the first tension bolt row was accurately predicted by the FE model. As shown in Fig. 3(c) and 3(d), the extended end-plate tests (EEP) revealed a common deformation pattern in a t-stub, involving the beam tension flange and the end-plate between bolt rows under tension, and this behavior was

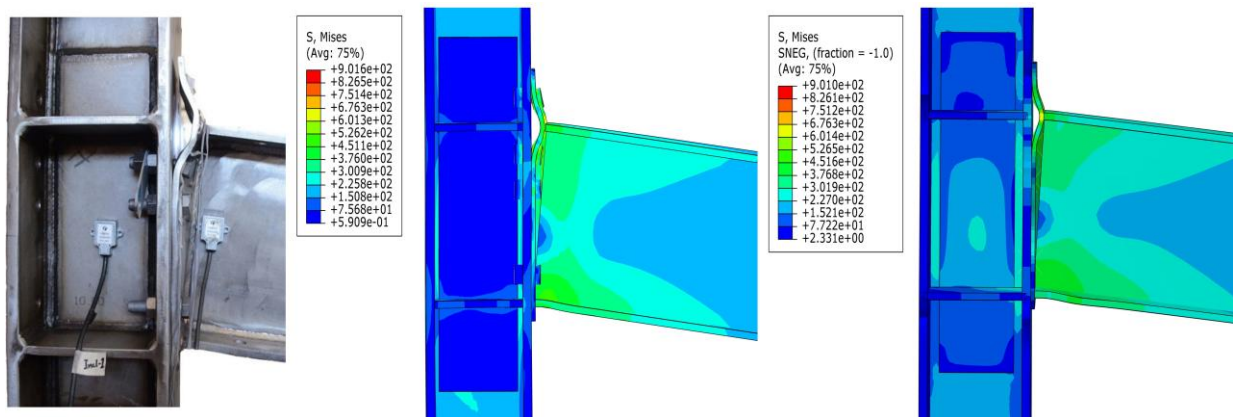
accurately replicated by the proposed model. Furthermore, the model effectively simulated the distinct bending of the column flange. The employed 3D solid method adequately replicated the neck profiles and fracture patterns of stainless-steel bolts and closely mimicked the experimental findings, as illustrated in Fig. 3(b) and 3(d). Moreover, the failure predictions of the shell models, relying on the fulfillment of specified failure criteria for the connector elements representing bolts, were in harmony with the experimental test results. This similarity underscores the high predictive accuracy of the suggested, simplified FE model when compared to its more complex conventional solid model counterpart.



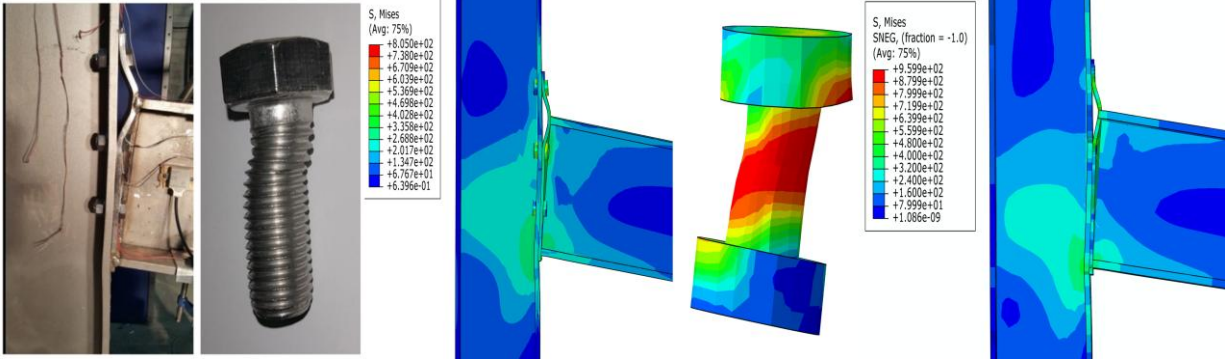
(a)



(b)



(c)



(d)

Fig. 3 Comparison of numerical and experimental failure modes (simplified shell models are displayed using rendering shell thickness feature): (a) FEP1 Test (Song et al.) [16] 3D solid model- FEP1 Simplified Shell model-FEP1; (b) FEP2 Test (Elfah et al.) [13] 3D solid model- FEP2 Simplified Shell model-FEP2; (c) EEP1 Test (Song et al.) [16] 3D solid model- EEP1 Simplified Shell model-EEP1; (d) EEP2 Test (Elfah et al.) [13] 3D solid model- EEP2 Simplified Shell model-EEP2.

To obtain the moment–rotation response of the analyzed connections, the moment is determined by multiplying the applied load at the beam end by the distance from this loading point to the column flange. Conversely, the joint rotation (Φ_{joint}) is characterized as the relative rotation between the centerlines of the upper and lower flanges of the beam at its endpoint and is defined by considering two primary components: first, the shearing rotation (Φ_s), which is predominantly influenced by the deformation of the panel zone of the column. Second, the gap rotation (Φ_{ep}), is a consequence of the relative deformation that occurred between the end-plate and the column flange. This relative deformation encompasses several factors: the bending deformation of the end-plate and the column flange and the elongation of the bolts. Φ_s , Φ_{ep} , and Φ_{joint} are determined in Eq. (7) [56]:

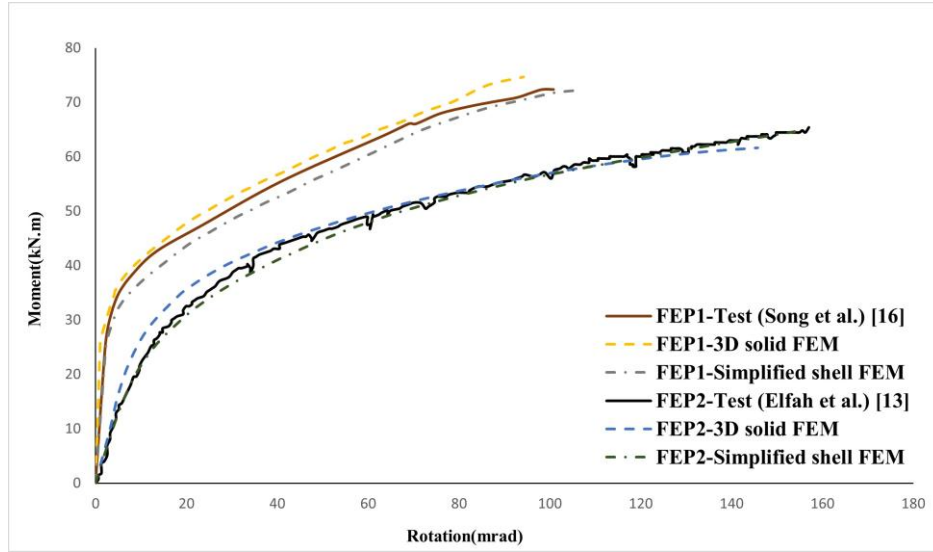
$$\Phi_s = \frac{\Delta}{h_t}, \quad (7a)$$

$$\Phi_{ep} = \frac{\delta}{h_t}, \quad (7b)$$

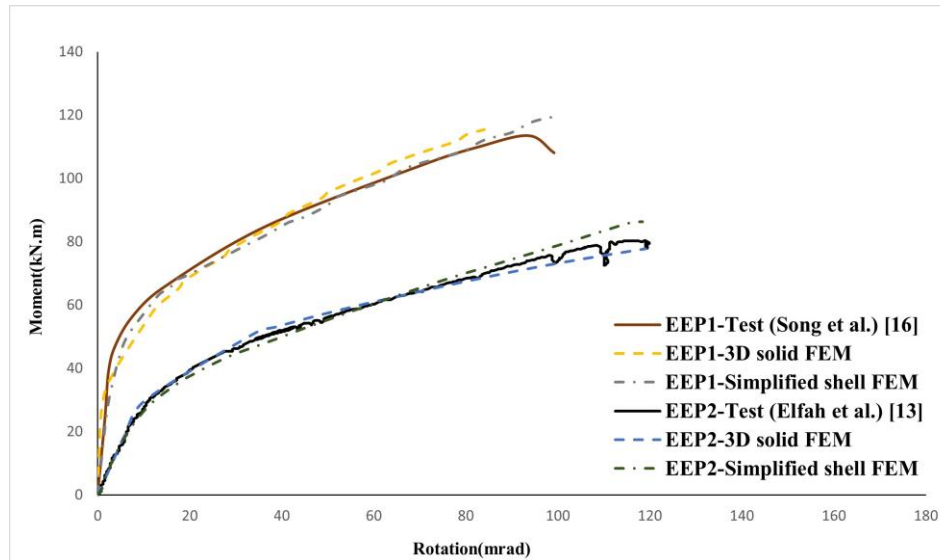
$$\Phi_{joint} = \Phi_s + \Phi_{ep}, \quad (7c)$$

where Δ signifies the difference in displacement between the panel zone's centerlines at the top and bottom flanges of the beam at its end. δ represents the space or gap existing between the end-plate and the column flange, specifically at the tension flange's centerline of the beam. Notably, h_t denotes the separation or distance between the centerlines of the top and bottom beam flanges.

Comparisons between numerical and experimental moment–rotation curves are illustrated in Fig. 4.



(a)



(b)

Fig. 4 Comparison of moment–rotation relationships: (a) flush end-plate joints; (b) extended end-plate joints

The minimal differences observed between the experimental, 3D solid, and 3D shell ($M-\Phi$) curves highlight the high predictive accuracy of the proposed simplified model. Both the 3D shell and 3D solid models successfully replicated the ($M-\Phi$) curves for various connection types, as shown in Fig. 4.

The following main characteristics obtained from the FE analysis results for the simplified shell model and the corresponding experimental ones were assessed from Fig. 4 and reported in Table 1: the plastic moment resistance $M_{j,R}$, which can be defined by the intersection of the two linear branches of the ($M-\Phi$) plot, the initial stiffness $S_{j,ini}$ (origin slope of the ($M-\Phi$) curve), the maximum moment capacity $M_{j,max}$, the ultimate rotational capacity $\Phi_{j,u}$. Considering Fig. 4 and the numerical values in Table 1, overall, a good agreement can be observed between the numerical model and the test data.

Table 1 Comparison of the predictions of the shell FEM model with the experimental results

Model	FE/experimental results
-------	-------------------------

	$S_{j,ini}$	$M_{j,R}$	$M_{j,max}$	$\Phi_{j,u}$
FEP1	0.96	0.97	0.99	0.98
FEP2	0.96	0.95	0.97	1.02
EEP1	0.85	1.09	1.05	1.06
EEP2	1.03	0.96	1.05	1.01

In this section, a straightforward and simplified model was developed to examine the data of stainless-steel bolted joints. This model required less than 15% of the computational time required by the conventional 3D solid model. The suggested modeling technique provides cost and time efficiencies, together with a high level of precision. These benefits can enhance the implementation of thorough numerical studies on stainless-steel joints.

4 Database generation

In the present study, the data set was created using FE simulations of stainless-steel beam-to-column connections. It contains 612 samples, each representing a unique set of connection properties. As seen in Fig. 5, the key geometric-related independent variables can be identified as end-plate thickness (t_{ep}), end-plate width (b_{ep}), end-plate height (h_{ep}), column flange thickness (t_{cf}), column web thickness (t_{cw}), column width (b_c), column depth (d_c), beam flange thickness (t_{bf}), beam web thickness (t_{bw}), beam width (b_b), beam depth (d_b), bolt diameter (D_b), The vertical distance from the innermost tension bolt to the innermost comparison bolt (P_i), spacing between bolts in tension (P_t), spacing between the comparison bolts (P_c) and horizontal distance between bolts (g_i).

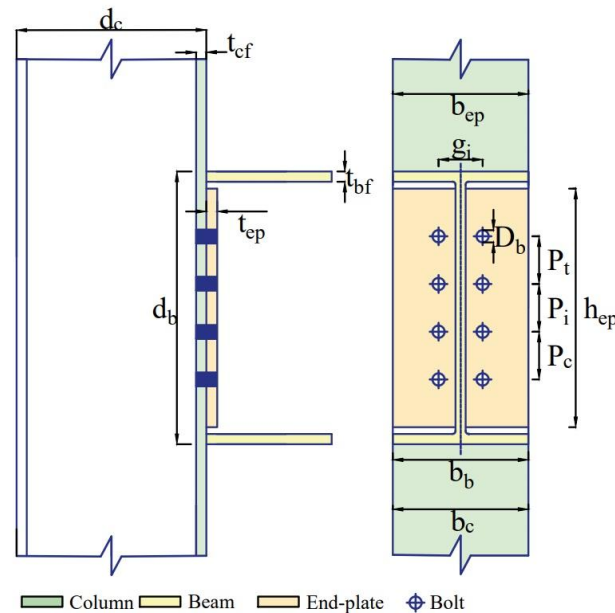


Fig. 5 General description of variables.

An extensive list of stainless-steel sections has been published by the British Stainless-steel Association [46]. In this directory, designers and specifiers can find diverse section types and sizes from a wide selection of suppliers [46]. In the first stage, all available stainless-steel sections were identified. Based on this, 88 welded

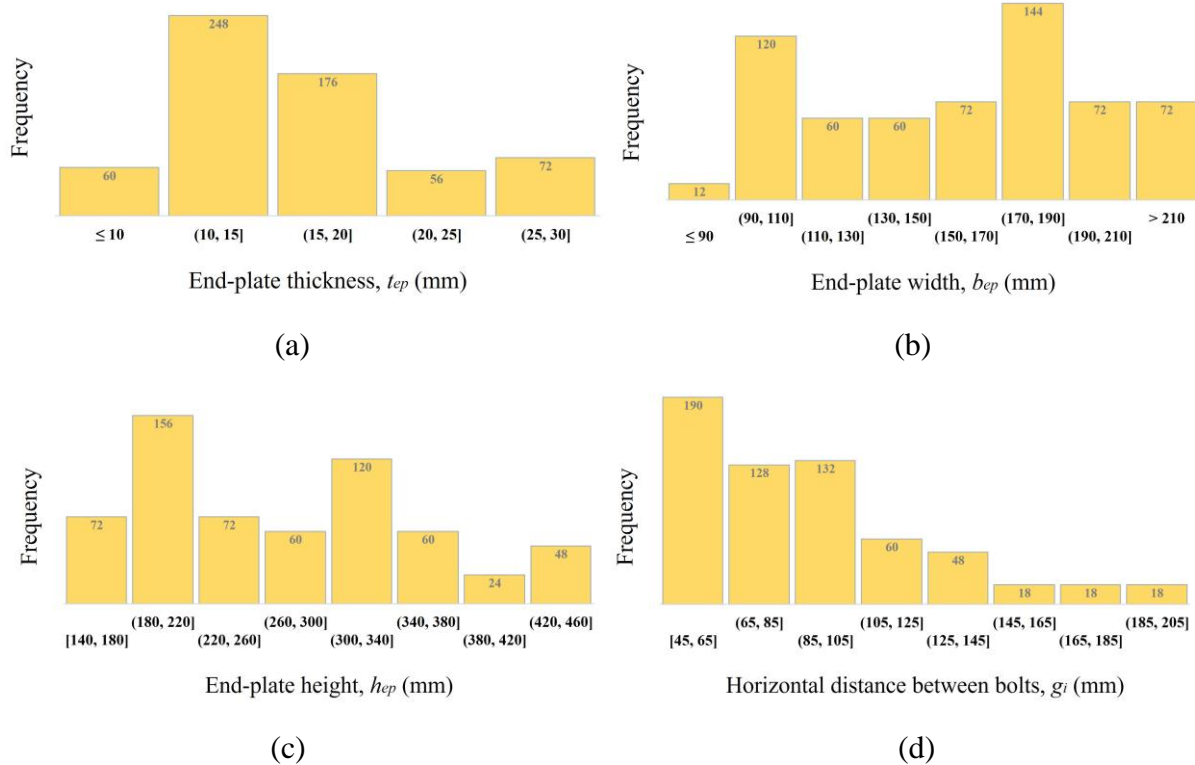
I-shaped beam sections and 62 H-shaped column sections from five different available suppliers were determined. However, all possible combinations of these sections are not practical. Therefore, only a subset of connections that are compatible with the specific criteria of the design guidelines presented in [Table 2](#) were carefully considered for this study.

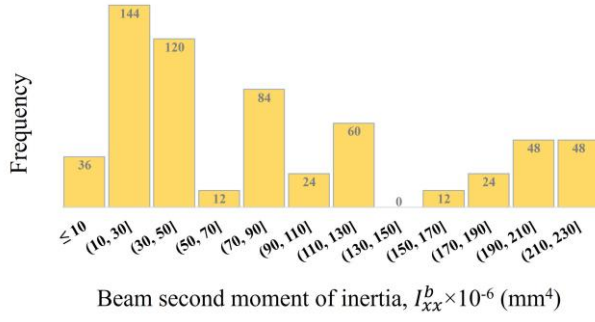
Table 2 Explanation of limitations being considered for the parametric study

Variables	Applicable criteria
b_b	$b_b \leq b_c$
d_b	$d_b \leq d_c$
$e_t, e_c^{3)}$	$1.2 d_0^{1)} \leq e_t \leq 4t^{2)} + 40$ mm
g_i	$2.4 d_0 \leq g_i, g_o \leq \min(14t, 200)$ mm
P_i, P_t, P_c	$2.2 d_0 \leq P_i, P_c, P_t \leq \min(14t, 200)$ mm

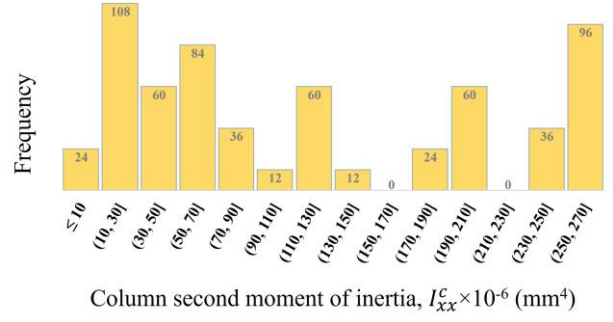
Notes: 1) d_0 : the hole diameter of a bolt; 2) t : the thickness of the thinner outer connected part; 3) e_t, e_c : the distance from the center of a fastener hole to the nearest end of a component, measured along and perpendicular to the direction of load transfer, respectively.

Lastly, after applying the aforementioned limitations and practical instructions for connection configuration, 612 samples were considered for analysis. [Figure 6](#) illustrates the statistical distribution of 10 considered features, where frequency represents the number of samples within the database.

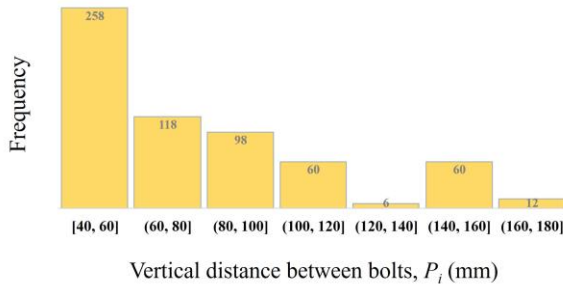




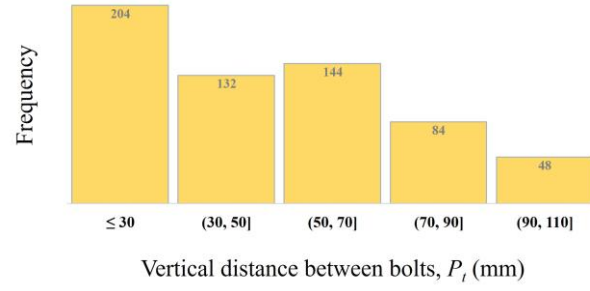
(e)



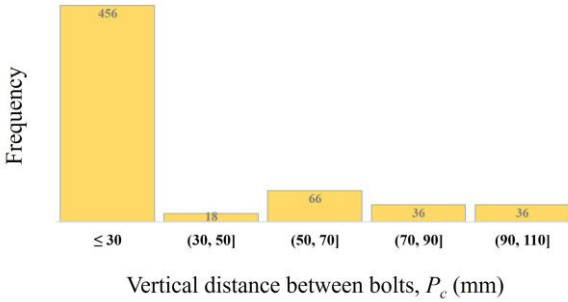
(f)



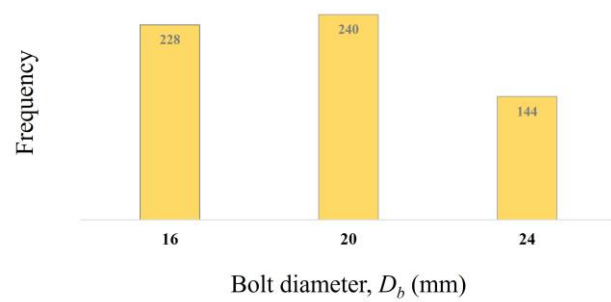
(g)



(h)



(i)



(j)

Fig. 6 Distribution of effective parameters considered for data generation phase: (a) End-plate thickness, t_{ep} (mm); (b) End-plate width, b_{ep} (mm); (c) End-plate height, h_{ep} (mm); (d) Horizontal distance between bolts, g_i (mm); (e) Beam second moment of inertia, $I_{xx}^b \times 10^{-6}$ (mm⁴); (f) Column second moment of inertia, $I_{xx}^c \times 10^{-6}$ (mm⁴); (g) Vertical distance between bolts, P_i (mm); (h) Vertical distance between bolts, P_t (mm); (i) Vertical distance between bolts, P_c (mm); (j) Bolt diameter, D_b (mm).

Table 3 Statistical distribution of input parameters

ID	Min	Max	Median	Mean	COV(%)
t_{ep} (mm)	6.0	30.0	15.0	17.0	32.1
b_{ep} (mm)	88.7	300.0	166.9	167.0	34.6
h_{ep} (mm)	140.0	426.4	270.0	276.7	29.6
g_i (mm)	45.0	200.0	85.0	91.3	39.5
P_i (mm)	40.0	165.0	70.0	81.3	42.3

P_t (mm)	0.0	100.0	50.0	43.5	78.4
P_c (mm)	0.0	100.0	0.0	18.5	178.0
D_b (mm)	16.0	24.0	20.0	19.5	15.8
$I_{xx}^b \times 10^{-6}$ (mm ⁴)	8.0	218.8	54.7	83.4	84.5
$I_{xx}^c \times 10^{-6}$ (mm ⁴)	8.4	262.3	78.7	117.5	77.9

The statistical distribution of the 10 considered input features is shown in [Table 3](#). Based on the information provided in this table, it can be stated that the considered samples have a wide range of geometric dimensions. Further, three layouts have been considered for placing bolts in the connection zone for a more detailed analysis (see [Fig. 7](#)).

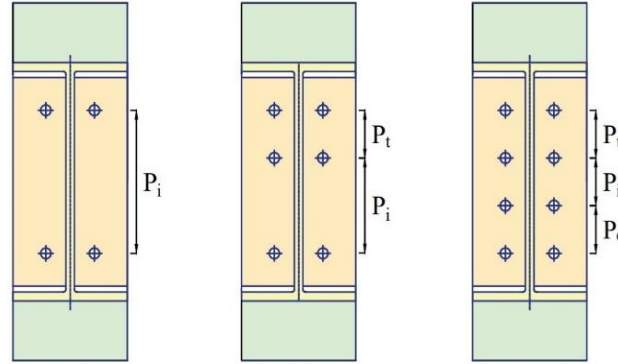


Fig. 7 Different bolt arrangements considered in this study.

5 Development of machine learning models

5.1 Machine learning algorithms

This study evaluates various ML models to assess their efficacy in predicting the behavior of stainless-steel FECs. The most accurate ML models are selected for the explanation of the ML results. The ML models were developed in this study with the use of the Scikit-learn ML package [57]. Eight models were implemented, including: DT, RF, KNN, GB, XGBoost, LGBM, AdaBoost, and CatBoost.

5.1.1 Decision Tree

DT is a supervised learning algorithm that is used for classification and regression. The algorithm works based on the hierarchical tree of conditions and decisions to be made known for its simplicity and clarity of the final results. The tree starts with a root node, which is a representation of the entire data set. At each step, the model evaluates all the existing conditions and divides the samples into separate nodes based on these factors. The model continued to split each group of data into smaller subgroups while creating new nodes and branches in each level based on the chosen values. The process of splitting or branching is continued repeatedly until the end points are pure in terms of classes or until some other stoppage criteria are met, like the minimum number of instances per node or the depth of the tree. The terminal nodes, or leaves, represent the end products or predictions of the model. Each leaf in the context of regression corresponds to a specific value. DTs are highly interpretable since the decision-making process diagram resembles a tree with branches and subbranches [58].

5.1.2 Random Forest

RF is a method of ensemble learning that improves the dependability and precision of predictions by combining the results of many DTs. This method is effective because it uses the strengths of a single DT

algorithm while avoiding its drawbacks. By using this approach, each tree is trained on a randomly chosen subset of the training data and on randomly chosen features, which brings variety to the model's predictions [59]. This process of splitting the data randomly, known as bootstrapping, ensures that each tree is exposed to a slightly different data set, thus reducing the likelihood of overfitting. RFs are formed by constructing individual DTs, all independently and in parallel, with each tree making its own decision. In regression problems, the final prediction is usually the average of the outputs from the trees. This accumulation of several models results in enhanced reliability and stability of the prediction since the variance is less and the prediction models are generalized for the unseen data. Additionally, the random subset selection of features at each split point in the trees prevents any single feature from dominating the model, further contributing to the overall diversity and reducing the risk of overfitting. This characteristic of RFs makes them more suitable for handling large data sets that have a high dimensionality and complex relationships between features [59].

5.1.3 K- Nearest Neighbors

KNN uses distances of the data points in feature space to make predictions of the outcomes. When making a prediction for a new data point, KNN uses the (k) nearest data points (neighbors) from the training set, with (k) being a predefined value. For regression problems, KNN predicts the value of the new data point as the average of the values of the (k) nearest neighbors [60]. This implies that the expected outcome is directly influenced by the values of the neighboring points, so that the prediction reflects the local feature space. KNN relies on the selection of a (k) value, and the distance function used to compute proximity. Some of the distance measures are the Euclidean measure, the Manhattan measure, and the Minkowski measure. The parameter (k) regulates the degree of locality of the decision boundary; small values of (k) can capture more detailed patterns in the data but are sensitive to noise, whereas large values allow for generalized predictions. KNN is simple and easy to understand and implement, but it can be time-consuming, especially when it is used on large data sets, since it involves computation of the distance between the new data point and all the points in the training data set [60,61]. However, KNN is still widely used because of its straightforward application and high efficiency in situations where the relationship between all the features and the target variable is complex and cannot be explained with the help of parametric models [60,61].

GB, XGB, LGBM, AdaBoost, and CatBoost are all use-ensembled boosting concept. These algorithms incorporate multiple weak learners, typically DTs, into one strong learner, boosting the learning process. Nonetheless, they differ in the implemented features that make them unique [58].

5.1.4 Gradient Boosting

GB is implemented through the steps of minimizing the loss function, such as the mean square error [62]. This method can be used through the following procedures. First, a basic model, for example, a decision tree with limited depth, is trained on the data set. This first model is known as a base learner. The residual errors, which are the differences between the predicted values and the actual values, are then calculated. In the subsequent steps, new models are trained to predict these residuals. Every new model is an effort to overcome the error made by the earlier models. The predictions of these new models are combined with the previous models' predictions to produce an updated model. This process is repeated for a predetermined number of iterations or until the residuals are minimized to an acceptable level. The term "gradient" in GB is therefore an implication of the gradient descent procedure used in the process of minimizing the loss function. In each iteration through the loop, the algorithm calculates the gradient of the loss function with respect to the model's predictions and updates the parameters. Thus, the algorithm effectively decreases the error in the model's predictions [62].

5.1.5 Extreme Gradient Boosting

XGBoost is a generalized Boosting algorithm based on the Gradient Boosting machine-learning framework, which is one of the most efficient algorithms in terms of predictive accuracy. Unlike the traditional gradient descent, which adjusts all the parameters across the whole data set, XGBoost improves the model iteratively by adding trees that address the mispredictions of previous ones. It uses gradient descent at every step, minimizing a custom loss function [63,64]. Furthermore, XGBoost incorporates other additional features to

boost performance, such as regularization techniques to prevent overfitting, parallelized tree construction to speed up computation, and sparsity awareness to handle missing data effectively [63].

5.1.6 Light Gradient Boosting Machine

LGBM is a fast ML algorithm that is developed using the gradient boosting technique. Two important algorithms that contribute to LGBM's speed and performance are Gradient-based One-Side Sampling (GOSS) and Exclusive Feature Bundling (EFB) [65]. GOSS enhances the training process by directing LGBM's focus on the most informative samples. This is achieved by retaining instances with large gradients, which are more likely to contribute to model accuracy, and randomly sampling from instances with small gradients. This means that the algorithm samples only some data, and in this way helps to reduce the amount of data that needs to be trained, thus making the training faster without necessarily having to reduce the accuracy of the data required. EFB decreases the size of the data by bundling mutually exclusive features, i.e., features that rarely take nonzero values simultaneously. It is a practical way of reducing the dimensionality of the feature space, making LGBM capable of handling large data sets. LGBM also uses the leaf-wise tree construction approach in contrast to the level-wise used by most traditional boosting algorithms. In a leaf-wise manner, LGBM builds trees by adding a leaf to the tree with the maximum loss reduction at each step [66]. This method can lead to deeper trees and, therefore, potentially better results on large data sets. But it must be done cautiously, as it can lead to overfitting, which is avoidable by applying proper constraints on the number of trees, the depth of trees, and other hyperparameters.

5.1.7 Adaptive Boosting

AdaBoost is a boosting technique that forms a strong model by combining several weak models or learners. Unlike some other boosting methods, AdaBoost is capable of modifying the weights of the samples that were mispredicted in the previous iteration such that the next models are more focused on these challenging samples [67]. This process continues until the model satisfies a certain level of convergence or the maximum number of iterations is reached. This reweighting mechanism enables the correction of the general model on the training set by diminishing the error rate. However, AdaBoost is more sensitive to noisy data and outliers than other boosting techniques [68]. Nonetheless, AdaBoost has received a lot of attention due to factors such as simplicity, efficiency and the capacity to improve the performances of weak predictors [69].

5.1.8 Categorical Boosting

CatBoost is a gradient boosting algorithm similar to XGBoost and LGBM but stands out due to its advanced handling of categorical data. It is designed specifically to process categorical variables efficiently through a technique that incorporates target-based statistics, reducing the risk of data leakage and overfitting that can occur with traditional encoding methods. CatBoost employs an ordered boosting method, which enhances model stability and accuracy [70].

Since the purpose of the section is not to examine all existing models in detail but only to provide an overview, more detailed information can be found in Refs. [62–70].

5.2 Data pre-processing

In this study, 612 samples (as explained in section 4) obtained from the FE analysis are used to train, validate and test the performance of ML predictions. Each data set consists of 10 features, namely (t_{ep}) , (b_{ep}) , (h_{ep}) , (g_i) , (p_i) , (p_r) , (p_c) , (D_b) , (I_{xx}^b) , (I_{xx}^c) and 4 outputs: $(S_{j,ini})$, $(M_{j,R})$, $(M_{j,max})$, $(\Phi_{j,u})$. To ensure the high efficiency of model training, in the beginning, the collected data were subjected to feature scaling to ensure the normalization of the features. Since the independent features represent different quantitative measures and dimensions, their values are scaled using the min-max scaler (Eq. (8)), a mathematical mechanism that normalizes the input features to the range of -1 and 1 :

$$x_n = \frac{2(x - x_{min})}{(x_{max} - x_{min})} - 1, (8)$$

In this context, x_n represents the normalized form of x , with x_{min} and x_{max} are the smallest and largest values of x observed, respectively.

This scaling was aimed to avoid that larger numerical values might dominate the learning process. The data were also checked for completeness, and no missing values were found. Outliers, or extreme values, were identified and managed to prevent their influence on the model. Then the prepared and scaled database was randomly divided into two parts, the training set and the test set. Such a method is commonly seen in building multiple ML models to allocate 80% of the data (489 joints) for the training set, using the “ k -fold cross-validation” refinement algorithm, leaving 20% for testing (123 joints). The testing data set was not perturbed and was not used for any type of training or validation; instead, it was only used as a means to independently assess the accuracy of the model.

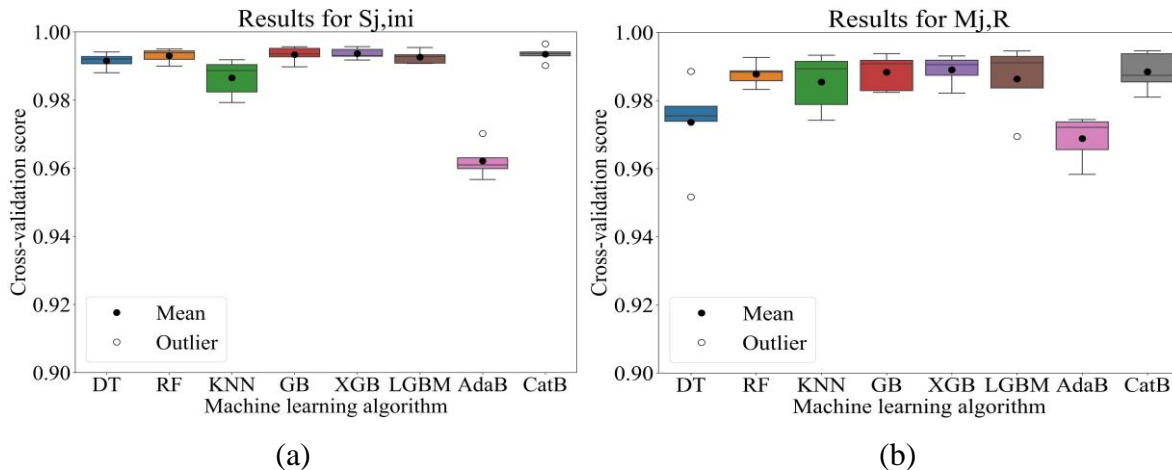
5.3 Model training

The initial model hyperparameters are found numerically following random search based on the training data set. This is then optimized using the grid search method. Subsequently, k -fold cross-validation algorithm is performed on the training data set [57]. In this technique, the training data set is split into K subsets. Then, the $(K-1)$ st subset of the whole data set is trained and the remaining is used to evaluate the performance of the model on a subset. This procedure is iteratively repeated K times, with each subset serving as the evaluation set once. The aim is to generalize the model-building process and avoid overfitting and sample biasness. Even though it is time-consuming and computationally intensive, especially when the search range is extensive, it has a high accuracy level, hence it is highly implemented in Ref. [70]. In this study, K is considered equal to 5. Hence, 5-fold cross-validation is performed for each ML algorithm, and the combination of hyperparameters with the maximum coefficient of determination (R^2) value is selected as the best combination. The main rationale behind this exhaustive process is to enable the algorithms to maximize predictive accuracy while maintaining strong generalizability and becoming less responsive to the overfitting problem.

5.4 Results and discussion

5.4.1 Cross-validation scores results

Figure 8 provides 5-fold cross-validation scores between the ML models derived for $S_{j,ini}$, $M_{j,R}$, $M_{j,max}$, $\Phi_{j,u}$ targets, respectively, where the box shows the range between the first and third quartiles, with a solid horizontal line representing the median. Additionally, the diagram’s whiskers extend to cover values up to 1.5 times the interquartile range. It was noted that outliers can be detected in some ML models like AdaBoost and CatBoost in Fig. 8(a), DT and LGBM in Fig. 8(b), DT, KNN, and AdaBoost in Fig. 8(c), and RF in Fig. 8(d). In general, ensemble algorithms like RF, XGBoost and GB showed very high median and mean values and tight boxes, which showed that they were consistently among the best performers. On the other hand, the AdaBoost algorithm had fewer narrow distributions of scores and gave lower performance than others.



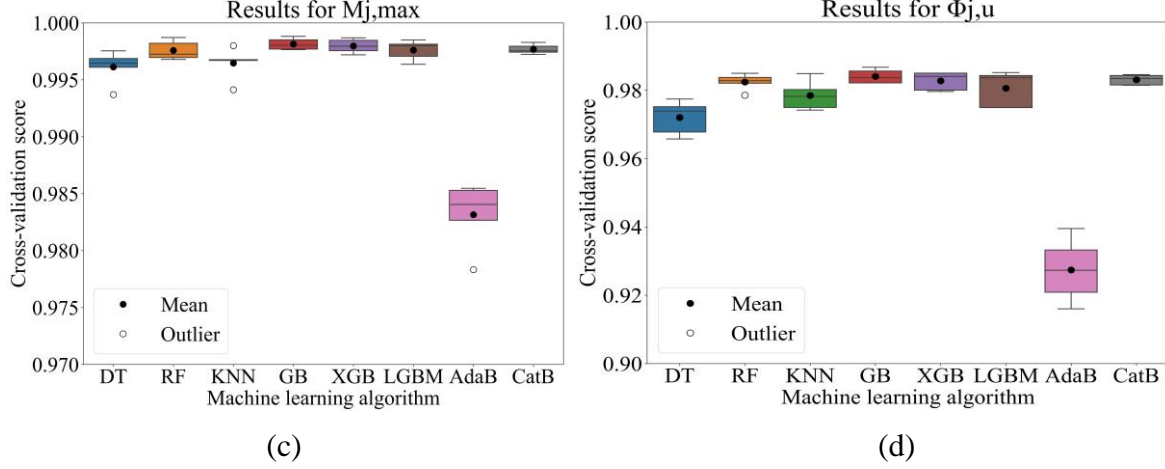


Fig. 8 Cross-validation scores: (a) $S_{j,ini}$; (b) $M_{j,R}$; (c) $M_{j,max}$; (d) $(\Phi_{j,u})$

5.4.2 Machine learning model performance evaluation results

In this paper, statistical criteria R^2 , Root Mean Square Error ($RMSE$), and Mean Absolute Error (MAE) were considered to measure the prediction error of ML models, and then the complete performance of the ML models is presented in [Table 4](#) for training, testing and all data sets. R^2 calculation determines how much variance in the dependent variable is predicted by the independent variable(s) ([Eq. \(9a\)](#)). $RMSE$ indicates, on average, how much the predicted values differ from the actual values by estimating the average magnitude of errors between predicted and actual values. It weighs larger errors more critically and it is calculated as the square root of the average squared difference between predicted and actual values ([Eq. \(9b\)](#)). MAE is a criterion for assessing the accuracy of a predictive model and it is calculated as the average of the absolute differences between predicted values and actual data ([Eq. \(9c\)](#)).

$$R^2 = 1 - \frac{\sum_{i=1}^n (y_i - \hat{y}_i)^2}{\sum_{i=1}^n (y_i - \bar{y})^2} \quad (9a)$$

$$RMSE = \sqrt{\frac{1}{n} \sum_{i=1}^n (y_i - \hat{y}_i)^2} \quad (9b)$$

$$MAE = \frac{1}{n} \sum_{i=1}^n |y_i - \hat{y}_i| \quad (9c)$$

Where y_i is the actual value, \hat{y}_i is the predicted value, \bar{y} is the mean of actual values, and n is the number of observations.

Table 4 (a) performance of predictive models for $S_{j,ini}$ output

Model	R^2			$RMSE$ (MN·m/rad)			MAE (MN·m/rad)		
	Train	Test	All data	Train	Test	All data	Train	Test	All data
DT	0.9926	0.9805	0.9926	0.7367	1.3362	0.7544	0.2109	0.5882	0.2631
RF	0.9960	0.9912	0.9954	0.5371	0.8965	0.5918	0.2525	0.4918	0.2923
KNN	0.9936	0.9841	0.9919	0.6809	1.2047	0.7843	0.1430	0.5797	0.2252
GB	0.9970	0.9909	0.9968	0.4662	0.9107	0.4921	0.2785	0.5565	0.3018
XGBoost	0.9971	0.9959	0.9970	0.4534	0.6103	0.4826	0.2563	0.4164	0.2812
LGBM	0.9970	0.9961	0.9969	0.4656	0.6012	0.4861	0.2615	0.4027	0.2833
AdaBoost	0.9645	0.9681	0.9655	1.6083	1.7099	1.6265	1.3571	1.7099	1.3712
CatBoost	0.9970	0.9923	0.9968	0.4632	0.8395	0.4954	0.2911	0.5225	0.3164

Table 4(a) compares the performance of ML models for predicting initial rotational stiffness ($S_{j,ini}$) based on R^2 , $RMSE$, and MAE metrics, considering training, testing, and all data sets. All models show high R^2 values, which suggest good prediction abilities of the models. The DT model has a satisfactory level of performance with stable R^2 (training = 0.9926, testing = 0.9805, all data = 0.9926) although it shows some overfitting with higher $RMSE$ and MAE in testing. The RF model displays a high R^2 (0.9960) in training and all data (0.9954) but drops in testing (0.9912). It shows $RMSE$ (0.5371, 0.8965) and MAE (0.2525, 0.4918) for training and testing data sets, respectively, which are slightly better than the DT model performance. KNN and GB models also have good performances with high R^2 values (0.9936, 0.9970) for training data sets, respectively, and reasonable $RMSE$ and MAE values. It can be seen that the GB model has slightly better results in the testing phase with a lower value of $RMSE$ (0.9107) as well as MAE (0.5565) than that of the KNN model. XGBoost and LGBM models also have high R^2 value (0.9970, 0.9969), respectively, in all data sets and show low errors. AdaBoost, however, yields the lowest R^2 (0.9655) for all data and the highest errors, which indicates the algorithm's inefficiency. The CatBoost model has an R^2 (0.9968) and low $RMSE$ and MAE , demonstrating strong overall performance. From all these, the XGBoost model is the best model with the highest R^2 for all data (0.9970) and relatively low $RMSE$ and MAE , which show the model's high predictive accuracy and generalization ability.

Table 4 (b) performance of predictive models for M_{iR} output

Model	R^2			$RMSE$ (kN·m)			MAE (kN·m)		
	Train	Test	All data	Train	Test	All data	Train	Test	All data
DT	0.9914	0.9895	0.9910	3.9954	4.4580	4.0948	2.5680	3.1963	2.6973
RF	0.9963	0.9921	0.9954	2.6246	3.8481	2.9158	1.4799	2.4162	1.6673
KNN	0.9954	0.9904	0.9947	2.9324	4.2476	3.1360	1.9853	2.9504	2.0929
GB	0.9957	0.9913	0.9948	2.8214	4.0618	3.1053	1.8347	2.5226	1.9665
XGBoost	0.9979	0.9917	0.9965	1.9933	3.9578	2.5392	0.6259	2.6629	1.0694
LGBM	0.9947	0.9926	0.9945	3.1500	3.7385	3.1999	1.9155	2.5896	1.9664
AdaBoost	0.9723	0.9753	0.9729	7.1791	6.8267	7.1097	5.7820	5.7404	5.7736
CatBoost	0.9972	0.9894	0.9962	2.2916	4.4772	2.6578	1.4362	2.8286	1.6311

According to **Table 4(b)**, the DT model shows high R^2 in the training set (0.9914) and all data sets (0.9910) but slightly lower in the test set (0.9895) with notable $RMSE$ (4.4580) and MAE (3.1963) values in test set, showing some overfitting. The RF model performs well with high R^2 (0.9963, 0.9954) in training and all data sets and low error of $RMSE$ (2.9158) and MAE (1.6673) for all data. KNN and GB models also show good performance with R^2 (0.9947, 0.9948) respectively, and relatively low $RMSE$ and MAE for all the data sets. The XGBoost model has the highest R^2 for all data (0.9965) and the lowest $RMSE$ (2.5392) and MAE (1.0694) which makes it the best model. The LGBM model also demonstrates good performance with R^2 (0.9945) and MAE (1.9664) for all data. The AdaBoost model has the lowest R^2 (0.9729) for all data, and the highest errors, which demonstrates it is the least suitable model for this data set. The CatBoost model gives rather good results with the R^2 (0.9962) for all data and reasonably good $RMSE$ and MAE values. In general, the XGBoost model has the highest R^2 , and the lowest $RMSE$ and MAE .

Table 4 (c) performance of predictive models for $M_{j,max}$ output

Model	R^2			$RMSE$ (kN·m)			MAE (kN·m)		
	Train	Test	All data	Train	Test	All data	Train	Test	All data
DT	0.9987	0.9936	0.9976	2.2413	5.1793	3.0640	0.6219	2.5653	1.0098
RF	0.9990	0.9975	0.9987	1.8915	3.2841	2.2329	1.0366	2.0606	1.2368
KNN	0.9989	0.9960	0.9984	2.0278	4.1219	2.5552	0.5557	2.7716	0.9776
GB	0.9994	0.9982	0.9991	1.4756	2.7343	1.8659	0.6819	1.8110	1.1136
XGBoost	0.9992	0.9976	0.9990	1.8042	3.1851	1.9994	1.1365	2.2262	1.2693
LGBM	0.9987	0.9971	0.9984	2.1921	3.4870	2.4921	1.2835	2.1823	1.4423
AdaBoost	0.9844	0.9842	0.9844	7.7851	8.1835	7.8668	6.6020	6.7779	6.6374
CatBoost	0.9994	0.9960	0.9991	1.5907	4.1003	1.8718	0.9577	2.3398	0.9227

In **Table 4(c)**, the performance of the DT model is very good in training and all data sets with high R^2 values (0.9987 and 0.9976) respectively, but the $RMSE$ and MAE values (5.1793, 2.5653) of testing data sets show overfitting. The RF model has the best fit with a high R^2 (0.9987) for all data and a low $RMSE$ (2.2329) as well as low MAE (1.2368), which indicates balanced and accurate prediction. KNN and GB models also show high

performance, with KNN and GB models having an R^2 (0.9984, 0.9991) for all data sets, respectively. Both have relatively low errors, showing that the data are well predicted. The XGBoost model has the highest R^2 (0.9990) for all data and relatively low $RMSE$ (1.9994) and MAE (1.2693), which confirms its high predictive accuracy. The LGBM model also has good performance, though its testing $RMSE$ (3.34870) is notably higher. The AdaBoost model underperforms; it has the lowest R^2 value (0.9844) for all data and the highest $RMSE$ and MAE , meaning it is less accurate. The CatBoost model, on the other hand, gives good results with the value of R^2 (0.9991) for all data and competitive $RMSE$ and MAE values. In general, the GB model delivers the highest R^2 (0.9991) and the lowest errors for all the metrics.

Table 4 (d) performance of predictive models for $\Phi_{j,u}$ output

Model	R^2			$RMSE$ (kN·m)			MAE (kN·m)		
	Train	Test	All data	Train	Test	All data	Train	Test	All data
DT	0.9903	0.9549	0.9879	6.6997	14.5973	7.4899	3.3896	8.3947	4.1006
RF	0.9942	0.9842	0.9923	5.1745	8.6359	5.9780	3.3779	6.2340	3.9100
KNN	0.9944	0.9810	0.9920	5.0767	9.4712	5.7476	3.2979	6.2697	2.3849
GB	0.9959	0.9864	0.9928	4.3793	8.0077	5.8011	1.4054	5.8497	3.7681
XGBoost	0.9930	0.9846	0.9921	5.6859	8.5393	6.0682	3.7912	6.1188	4.0615
LGBM	0.9921	0.9857	0.9913	6.0415	8.2132	6.3626	4.1833	6.2833	4.5076
AdaBoost	0.9294	0.9240	0.9286	18.0665	18.9532	18.2173	15.2156	15.5769	15.2686
CatBoost	0.9938	0.9823	0.9923	5.3552	9.1441	5.9872	3.5154	6.5686	3.9331

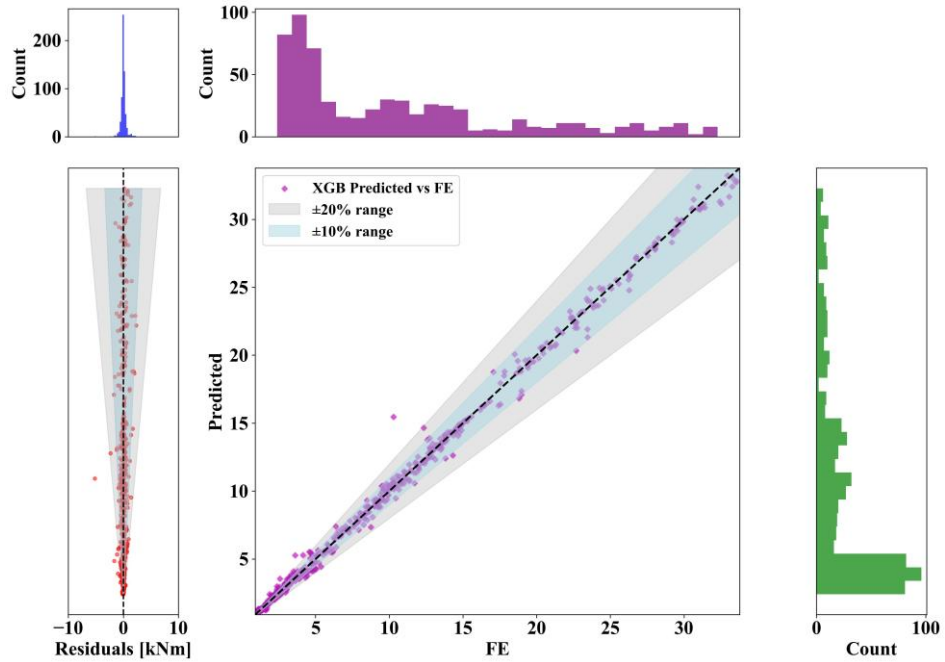
From **Table 4(d)** it can be seen that the DT model has a high value of R^2 for training data (0.9903) and all data (0.9879) but for the testing data the significantly lower R^2 , and higher $RMSE$ and MAE (0.9549, 14.5973, and 8.3947), respectively, which shows that there is a high degree of overfitting. The RF model gives a good fit with high values of R^2 (0.9923) for all data, low $RMSE$, and MAE (5.9780, 3.9100) respectively, which indicates high predictive ability. The KNN model also gives satisfactory results with an R^2 (0.9920) and relatively low $RMSE$ (5.7476) and MAE (2.3849), proving the models high accuracy in all data. GB model again has the highest R^2 (0.9928) for all data, and relatively low $RMSE$ (5.8011) and MAE (3.7681), which shows that the model is well balanced and provides accurate predictions. The XGBoost model maintains very good results with an R^2 (0.9921) for all data, though with higher $RMSE$ (6.0682) and MAE (4.0615) compared to other models. The LGBM model has the highest R^2 , equal to 0.9913 for all data, but there is some performance variability in $RMSE$ (6.3626), and MAE (4.5076). The AdaBoost model significantly underperforms, with the lowest R^2 values (0.9286) for all data and the highest $RMSE$ and MAE . The CatBoost model also shows good results with an R^2 (0.9923) for all data and competitive $RMSE$ and MAE values. Among these models, the GB model is the best model, as it gives the highest R^2 and the least error for this data set.

The performance differences between XGBoost and GBoost in this study can be attributed to both model architecture and the specific requirements of each target prediction. XGBoost with parallel processing and efficient regularization techniques was best suited for the prediction of initial rotational stiffness ($S_{j,ini}$) and plastic moment resistance ($M_{j,R}$). These outputs needed modeling of interactions between feature characteristics, which XGBoost achieved by reducing overfitting and increasing accuracy due to its regularization and learning rate adjustments. On the other hand, GBoost, which constructs trees in sequence, was more accurate in predicting maximum moment resistance ($M_{j,max}$) and ultimate rotation capacity ($\Phi_{j,u}$). This type of learning process enabled GBoost to capture these gradual changes in the data, which are characteristic of these outputs. The tree structures developed by GBoost allowed for the capture of the necessary detail to enhance the predictive accuracy of these target variables. Selecting models based on these strengths allowed the study to provide the best match between each target and the model that would provide the most accurate and reliable result.

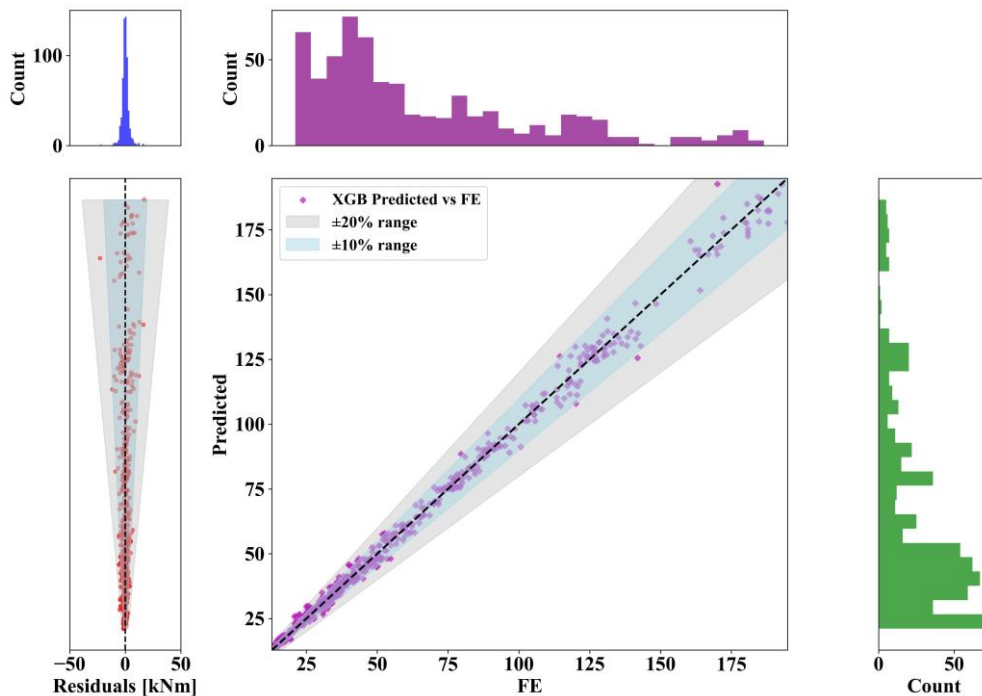
5.4.3 Comparison of actual vs predicted results

Figure 9 gives an overview of the assessment of the best performing ML models for output responses. Each sub-figure comprises several components: The bottom center panel shows the scatter plot of predicted vs. FE values, with shaded regions representing $\pm 10\%$ and $\pm 20\%$ error ranges. The bottom left panel depicts the residual errors of the model. The histograms illustrate the distributions of residual errors (top left panel), FE

values (top right panel), and predicted values (bottom right panel). For all target outputs, the center scatter plot demonstrates a close adherence of the predicted values to the base 1:1 line, which means high correlation between the calculated and actual value. The $\pm 10\%$ and $\pm 20\%$ error lines are shown for comparison to the level of accuracy attained, and as seen, the majority of the values are within the shaded area when all four target responses are taken into consideration. The residual histogram and the residual plot are centered at zero, implying minimal systematic bias and that the errors are randomly distributed. Overall, the models can give accurate and unbiased prediction with minimal scatter across the entire data set, as shown in Fig. 9; thus affirming the reliability of the best performing models.



(a)



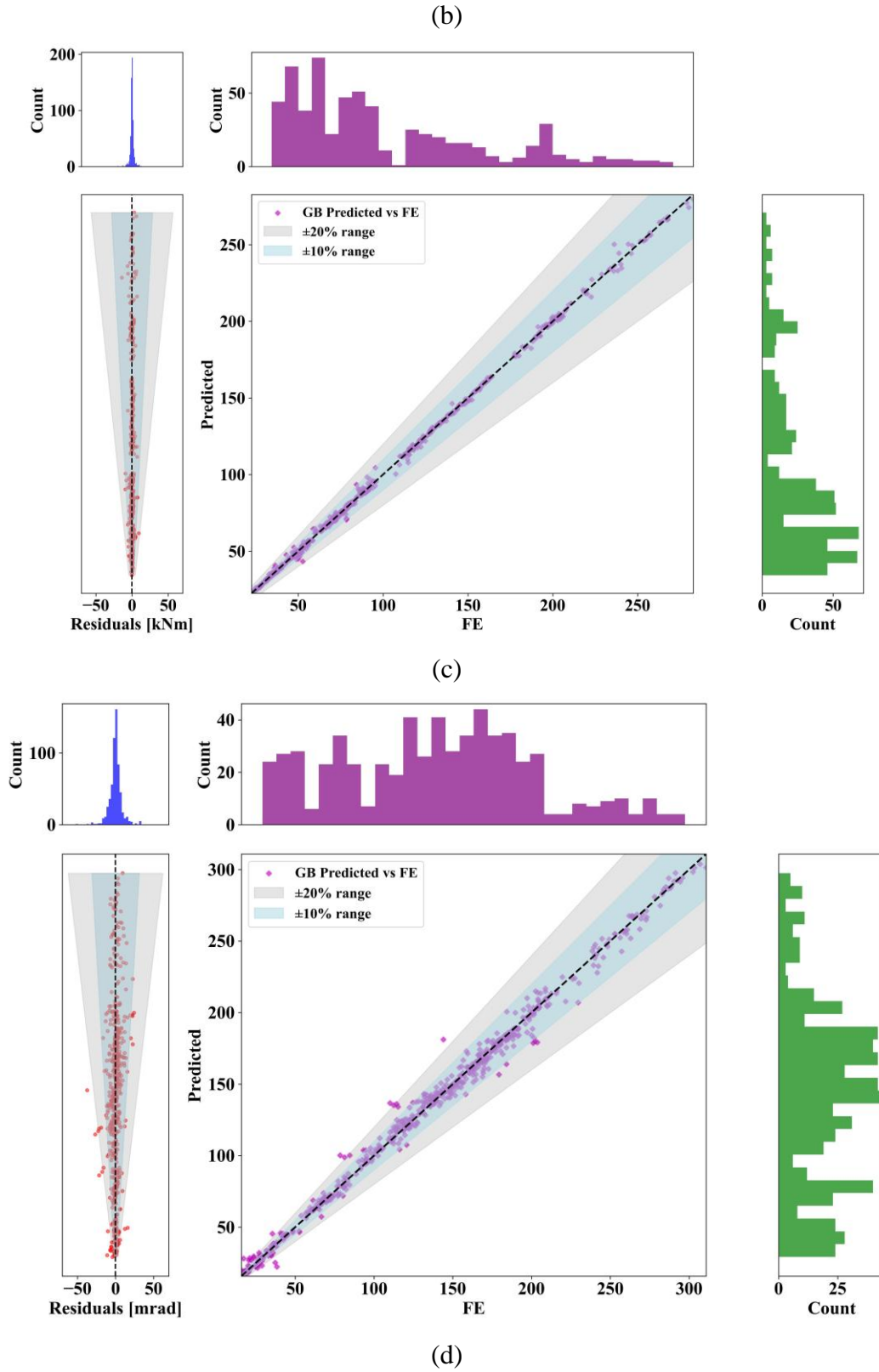


Fig. 9 Comparison of the best-performing ML models' actual and predicted outcomes for each target response: (a) initial rotational stiffness ($S_{j,ini}$); (b) plastic moment resistance ($M_{j,R}$); (c) maximum moment resistance ($M_{j,max}$); (d) rotational capacity ($\Phi_{j,u}$).

5.4.4 Selected hyperparameter optimization results for Extreme Gradient Boosting algorithm

The precise calibration of hyperparameters is vital to the successful execution of ensemble learning models. In this section, due to space constraints, only a subset of the hyperparameter optimization results for the selected XGBoost model in predicting the $S_{j,ini}$ output is presented. As explained in section (5.3), to analyze and optimize hyperparameters, the Gird search function was used. For a range of critical hyperparameters, such as the maximum depth of a tree, the number of estimators, and the learning rate, which are considered to have the greatest influence on model output, Fig. 10 illustrates the performance of the XGBoost model in predicting $S_{j,ini}$. Figure 10 plots four different levels of learning rate for three different values of maximum depth. These graphs show the RMSE measurement index on the vertical axis and the number of trees ($n_estimator$) on the horizontal axis. As can be seen in Fig. 10, learning rate and tree number are inversely related, and increasing learning rate results in fewer trees being required for optimal performance. In addition, increasing the number of trees enhances the accuracy of the model prediction. Additionally, models with higher learning rates performed better at all levels of maximum tree depth when considering the same number of trees. As for the XGB model, the lowest errors were obtained with $n_estimators = 100$, $max_depth = 4$, and learning rate = 0.2 (Fig. 10).

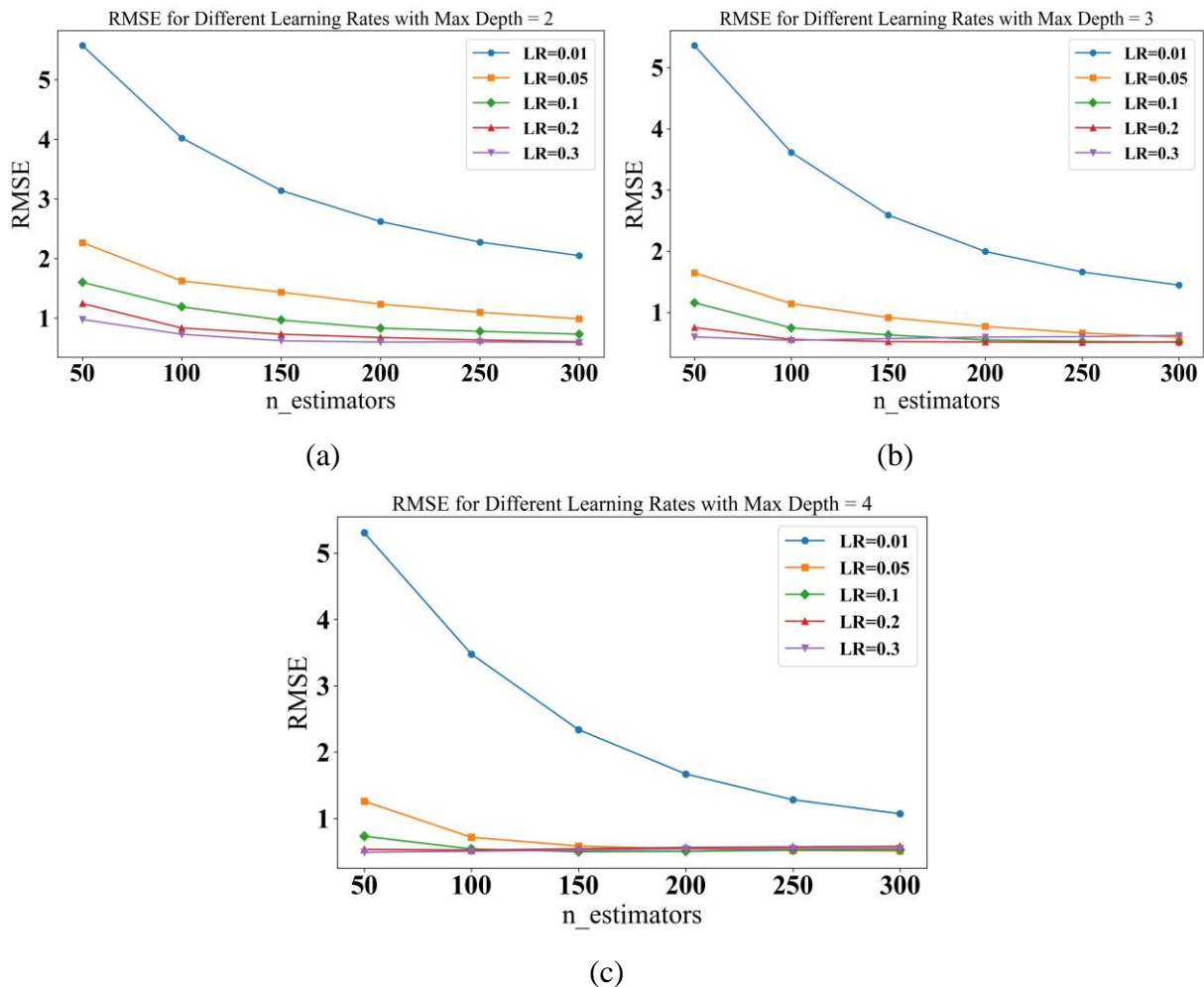


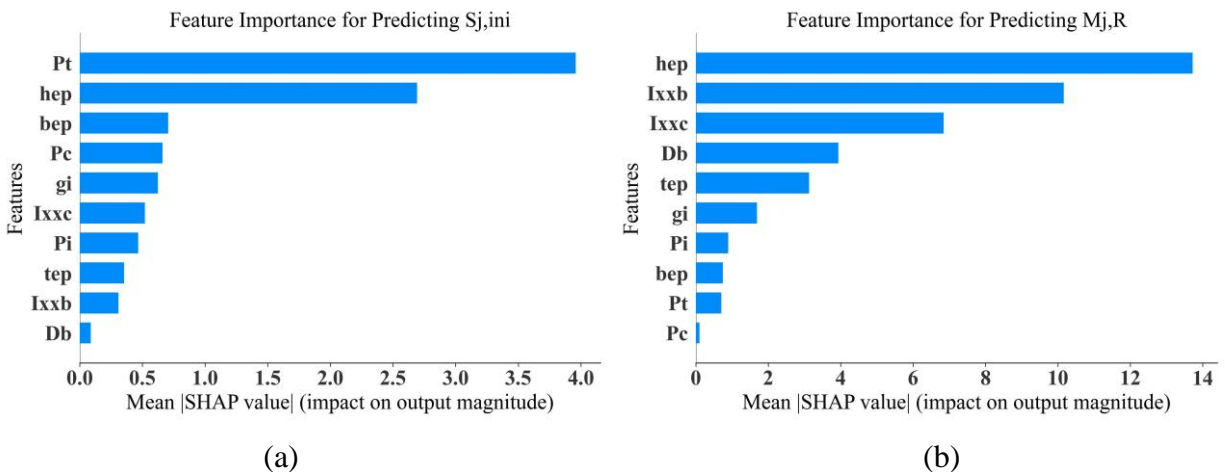
Fig. 10 Optimizing hyperparameters for XGBoost training across diverse learning rates : (a) Max depth =2; (b) Max depth =3; (c) Max depth = 4

6 Explainable Machine Learning method

In the field of EML, the attempt to explain the decision-making processes of algorithms, traditionally perceived as impenetrable “black boxes,” has led to the emergence of two fundamental methodologies: model-agnostic and model-specific methods [71]. The latter explores the internal algorithms of specific ML models and focuses on their structure to get an internal perception to build explanations. In contrast, model-agnostic methods established a universal approach that is efficiently usable across the different ML-architecture. SHAP is a model-agnostic explanation technique [72–75] that can be picked as well-known among them. SHAP is to be highlighted for its double character of global and local observations in the process of model decision-making [71]. It allows interpreting the behavior of a model by understanding the link between the model’s input features and output targets. More precisely, the Shapley Additive Explanation has contributed to the ML community by pointing to the exact weight of features for individual prediction. In this theoretical construct, the model is similar to the rule sets of games and features are equated to the players who might either partake in the game (when the feature is observed) or abstain (when the feature is unobservable). By this metaphor, the calculations of the Shapley values are realized based on the assessment of the model by different input feature combinations. This paper first assessed eight different ML models: DT, RF, KNN, GB, XGB, LGBM, AdaBoost, and CatBoost. The assessment results of these models are represented in Table 4. Accordingly, for SHAP analysis, the best-performing ML models were selected. The XGBoost model was chosen for predicting $S_{j,ini}$, $M_{j,R}$, along with GBoost for $M_{j,max}$ and $\Phi_{j,u}$.

6.1 Feature importance analysis

Figure 11 shows a hierarchy of input variables based on the measure of the influence on the predictive accuracy of the XGBoost model for $S_{j,ini}$ and $M_{j,R}$, as well as the GBoost model for $M_{j,max}$ and $\Phi_{j,u}$ outcomes. The mean absolute SHAP value assesses the significance of each feature, so a higher value indicates a stronger influence. Therefore, based on Fig. 11(a) P_t considered the most significant variable, followed by h_{ep} , and then the I_{xx}^c . Precisely, P_t has the mean absolute SHAP value of 3.12, h_{ep} : 2.65, and I_{xx}^c : 0.98, which rates as 31%, 26.49%, and 9.84% of the aggregated mean absolute SHAP value across all features. The next features contribute nearly 5% each to the overall mean absolute SHAP value, and I_{xx}^b and D_b account less than 2% each. As represented by Figs. 11(b) and 11(c), the top five most important features are: I_{xx}^b , h_{ep} , I_{xx}^c , D_b , and t_{ep} , tally to over 90% of the relative mean absolute SHAP value. Conversely, as represented by Fig. 11(d), P_t , I_{xx}^c , and D_b are the three primary features, with mean absolute SHAP values of 34.21, 20.27, and 14.37, respectively, and with percentages of 33.96%, 20.12%, and 14.27% in the overall significance. The following P_i , h_{ep} , and g_i contribute over 20% significance, while the influence of the last four features is comparably lower, summing to less than 10%.



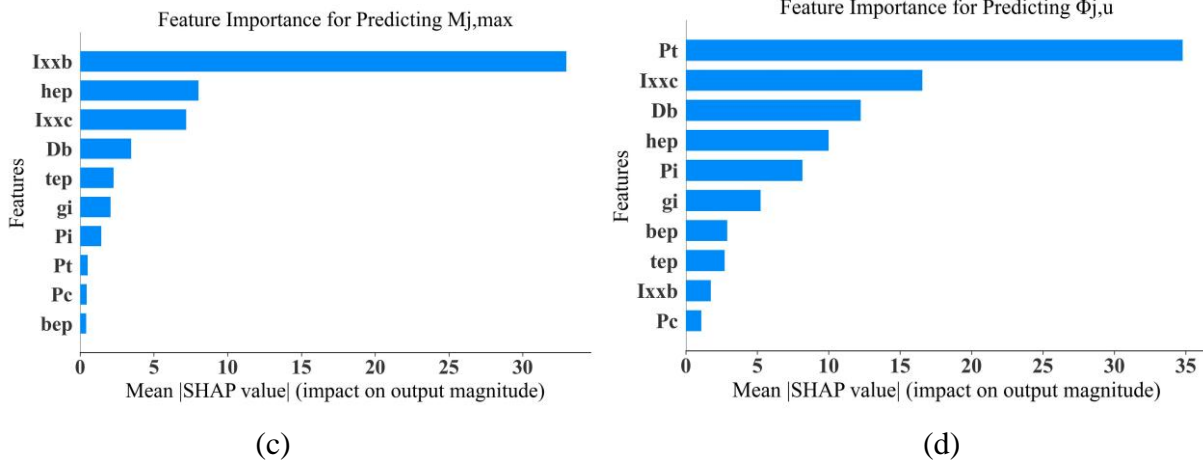
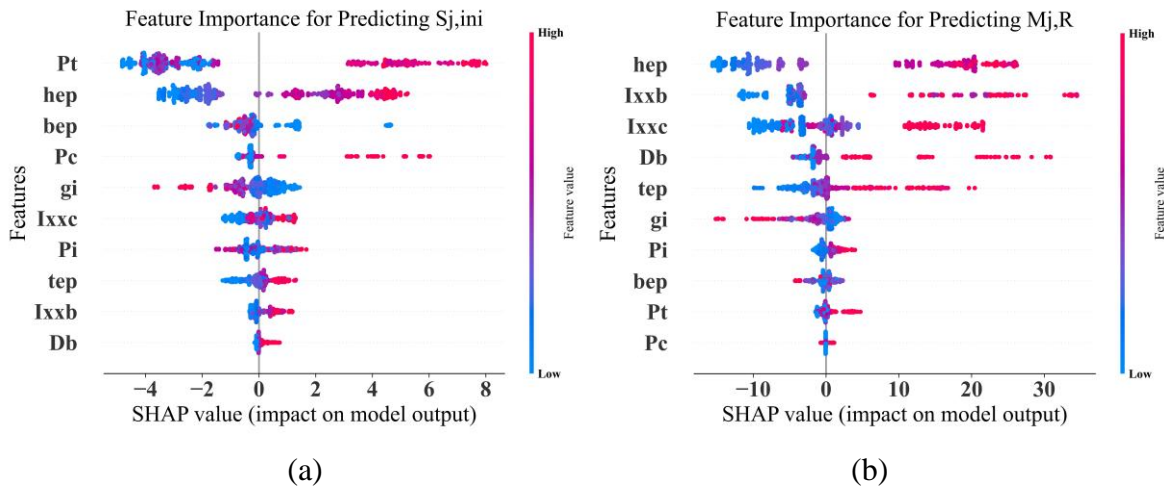


Fig. 11 Feature importance plots of the top performing model: (a) $S_{j,ini}$; (b) $M_{j,R}$; (c) $M_{j,max}$; (d) $(\Phi_{j,u})$

6.2 Global explanation

Figure 12 shows additional important results that is not readily apparent in the input feature importance plot of Fig. 11. The SHAP summary plot illustrated in Fig. 12 reveals the correlation between the input features and the target outputs so that each input feature can be classified into positive, negative, or no clear correlation with the target outputs. In the “SHAP summary plot” a color gradient is applied to display the range of values, where red shows higher and blue signifies lower values of each input feature. As Fig. 12(a) shows, most input features have a positive correlation with the initial rotational stiffness ($S_{j,ini}$), with the exception of g_i and b_{ep} , which show a negative correlation and their increase tends to decrease the predicted values. Figures 12(b) and 12(c) show that the top five features are significant and also have a positive correlation with the values of plastic moment resistance ($M_{j,R}$) and maximum moment resistance ($M_{j,max}$) of the joint. This indicates that an increase in these input features is associated with an increase in the predicted values of $M_{j,R}$ and $M_{j,max}$. This is expressed via the red dots that are mostly located in the areas where the SHAP values are above the zero line. A negative association for features like P_t , I_{xx}^b , P_i , h_{ep} , and t_{ep} can be noticed with the ultimate rotation value ($\Phi_{j,u}$) in Fig. 12(d). This suggests that an increase in these features results in a decreased rotation capacity.



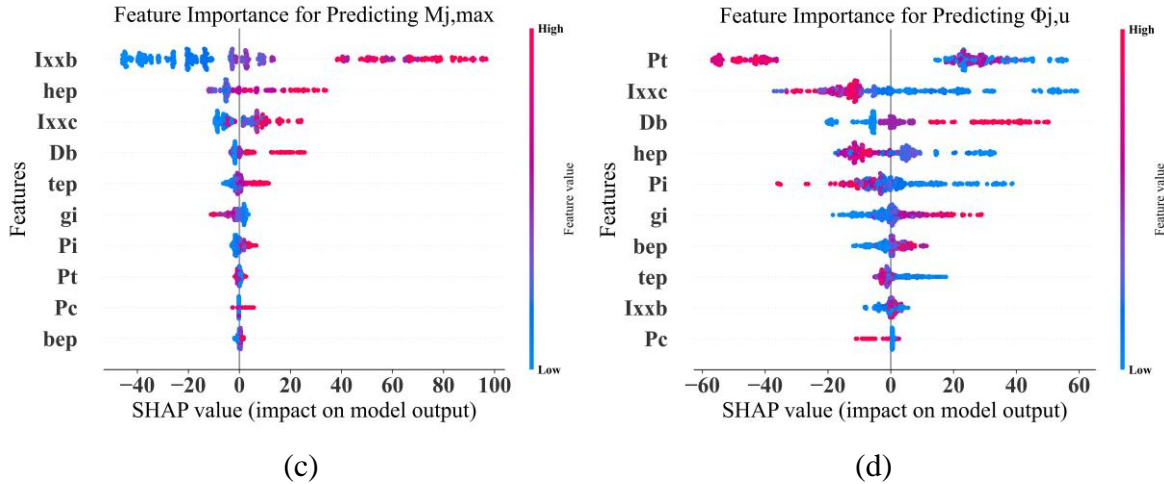
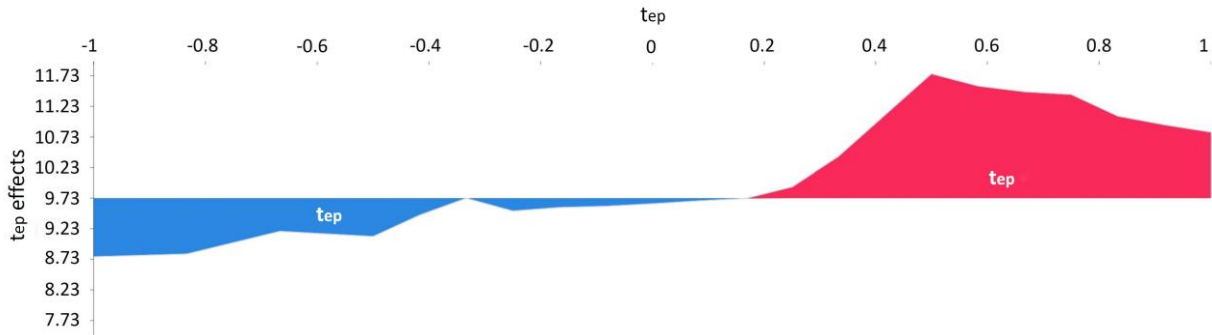
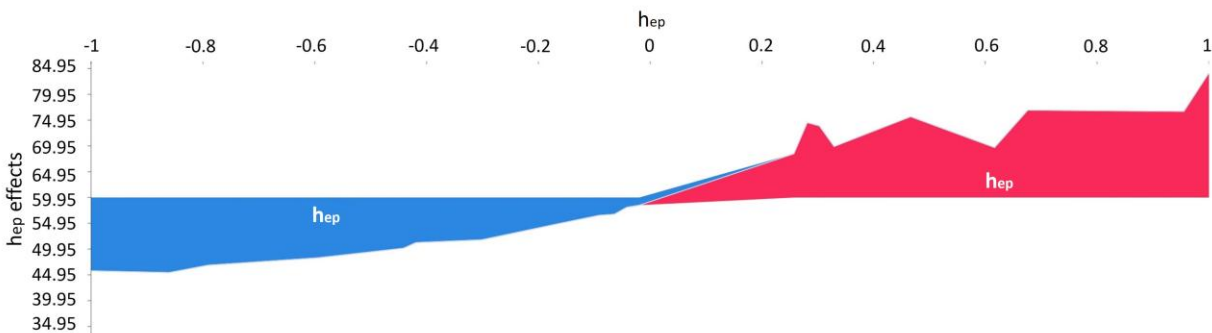


Fig. 12 Shap summary plots: (a) $S_{j,ini}$; (b) $M_{j,R}$; (c) $M_{j,max}$; (d) $(\Phi_{j,u})$

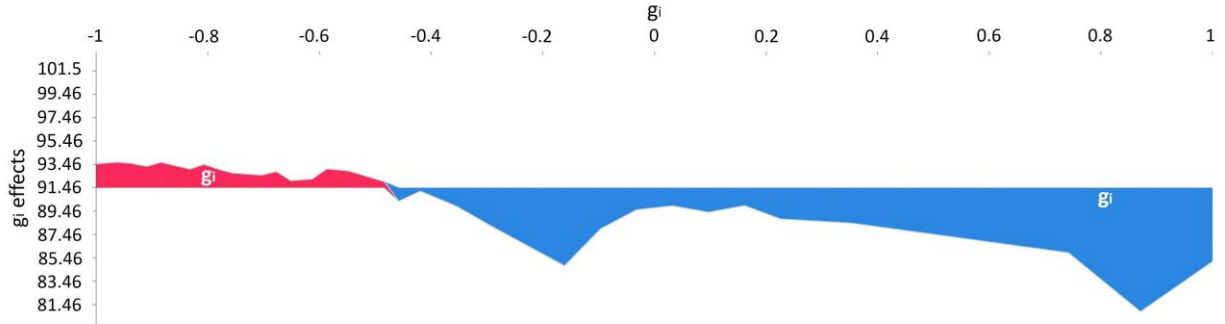
Figure 13 depicts the effect of selected input features t_{ep} , h_{ep} , g_i , and I_{xx}^c on predicting $S_{j,ini}$, $M_{j,R}$, $M_{j,max}$, and $\Phi_{j,u}$ target outputs, respectively, by means of SHAP force plots. SHAP force plot offers more detailed explanations, in which the y-axis shows the average impact of the chosen features, which are aligned along the x-axis. The red areas reflect regions where the chosen input features have a significant impact on driving the prediction above the base value (the average value of the data set). In contrast, the blue areas indicate regions where the selected input features cause the prediction to decrease below the base value. Figure 13(a) demonstrates that when the scaled value of t_{ep} is less than approximately 0.2, it results in a reduction in the predicted initial rotational stiffness from the baseline value of 9.73 MN·m/rad. In contrast, values of t_{ep} exceeding 0.2 positively influence the prediction, leading to an increase in the initial rotational stiffness estimate.



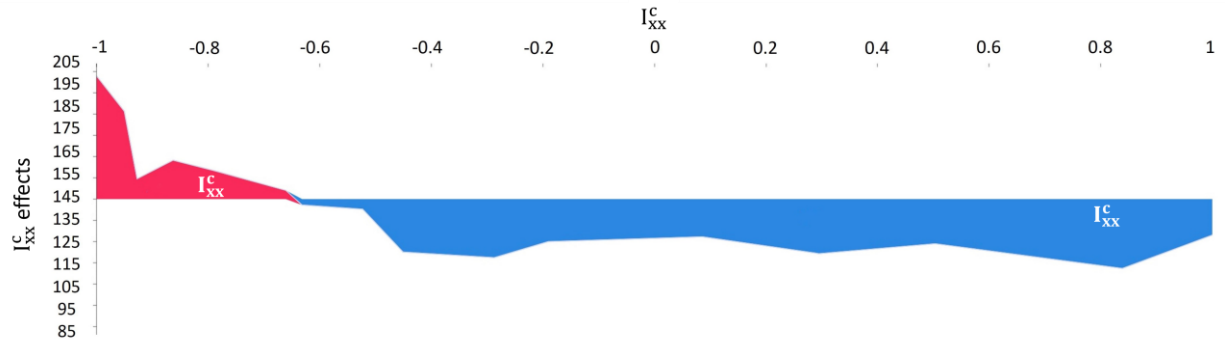
(a)



(b)



(c)



(d)

Fig. 13 SHAP force plot for: (a) t_{ep} ; (b) h_{ep} ; (c) g_i ; and (d) I_{xx}^c features.

6.3 Local explanation

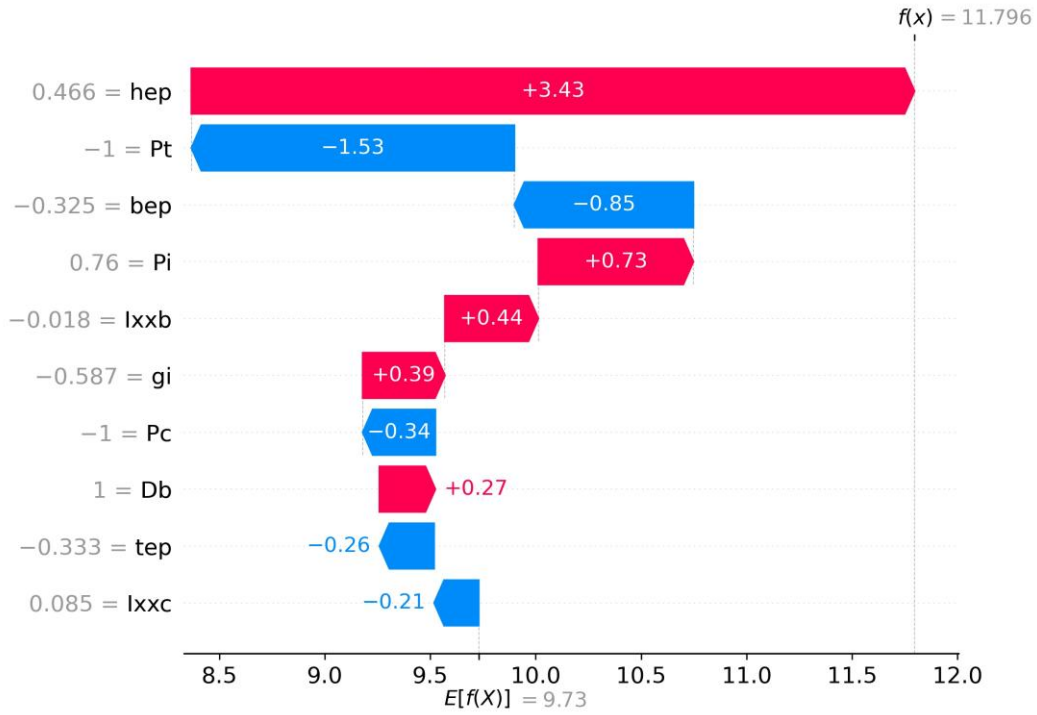
Visual representations of the SHAP values for individual samples were also provided in this section. The model's predictions for SHAP across various samples were illustrated in Figs. 14 and 15 using waterfall plots and individual SHAP force plots. These plots were focused on the prediction of initial rotational stiffness ($S_{j,ini}$) and the ultimate rotation of connections ($\Phi_{j,u}$), respectively. As the plots were based on scaled features, the actual geometrical descriptions of the chosen samples are detailed in Table 5.

Table 5 Actual geometrical descriptions of the chosen samples

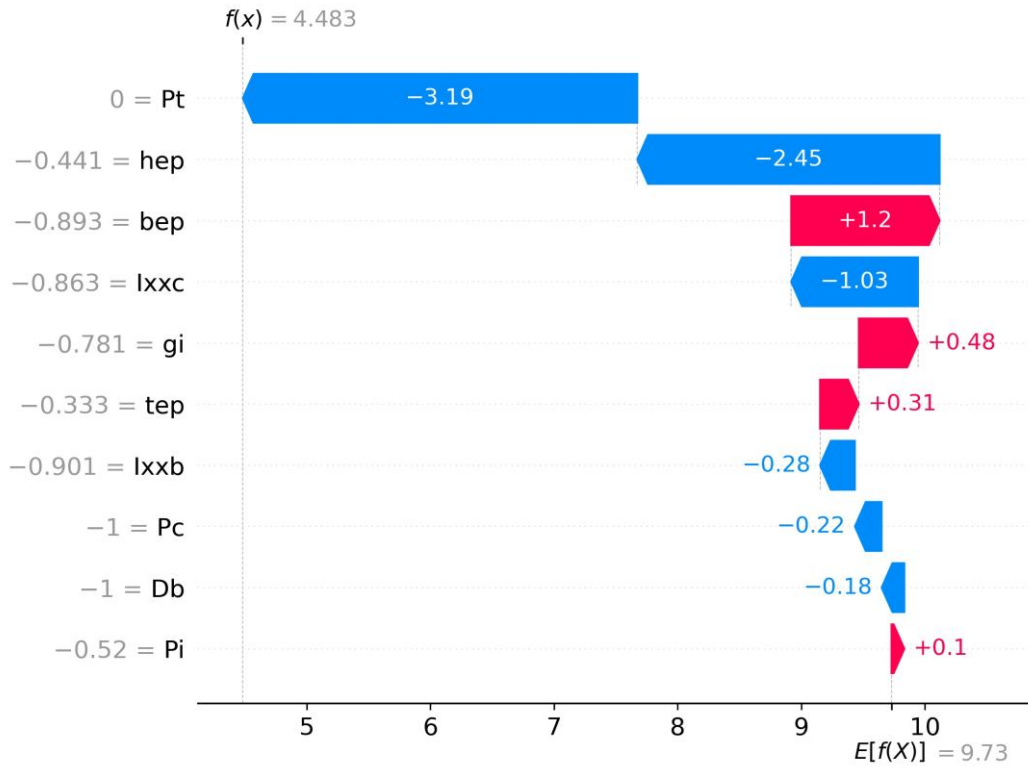
ID	t_{ep} (mm)	b_{ep} (mm)	h_{ep} (mm)	g_i (mm)	P_i (mm)	P_c (mm)	D_b (mm)	I_{xx}^b (mm)	I_{xx}^c (mm)
10	14	160	350	77	150	0	24	1.46E + 08	1.11E + 08
70	15	160	350	77	160	0	24	1.46E + 08	1.11E + 08
145	29	300	320	200	60	60	20	2.42E + 08	2.1E + 08
169	14	100	220	62	70	50	16	2.58E + 08	1.85E + 08
253	26	177.7	422.6	80	90	90	24	2.62E + 08	1.84E + 08
347	15	165	323.4	100	95	0	24	1.99E + 08	83702368
440	10	114	140	58	45	0	16	8.38E + 06	7.98E + 06
459	14	101.6	274	63	80	80	16	5.14E + 07	2.77E + 07

The SHAP waterfall plot breaks down the prediction of initial rotational stiffness into the contributions of each input feature, as shown in Fig. 14(a)–14(d). This plot type is specifically intended to clarify the prediction for an individual instance, requiring a single row from an explanation object as input. The construction of waterfall plots is aimed at visualizing the prediction individually. The plot begins at the bottom with the

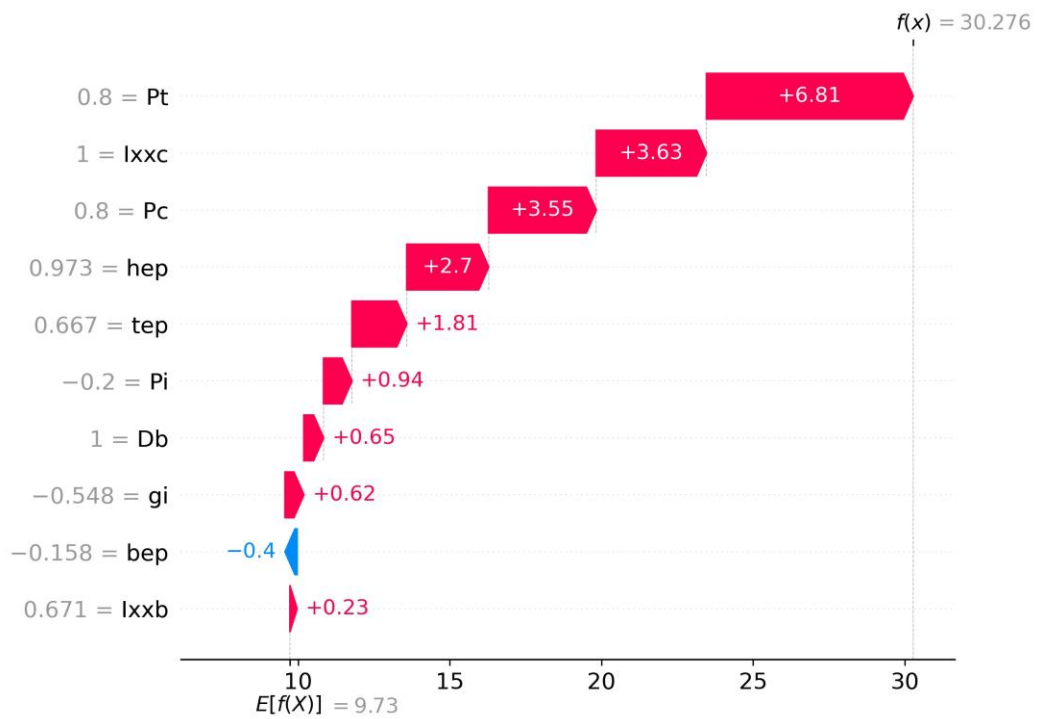
model's expected value output, and each subsequent row displays either a positive (in red) or negative (in blue) influence from each of the 10 features, incrementally adjusting the value from the expected output to the specific model output for the given prediction. For instance, in Fig. 14(a), the waterfall plot's baseline starts with the model's expected output value, $E[f(x)] = 9.73$ MN·m/rad which depicts the global predicted average of $S_{j,ini}$. Then, incrementally, this value is adjusted to reach the predicted output value, $f(x) = 11.796$ MN·m/rad, which is close to the actual value of 11.983 MN·m/rad.



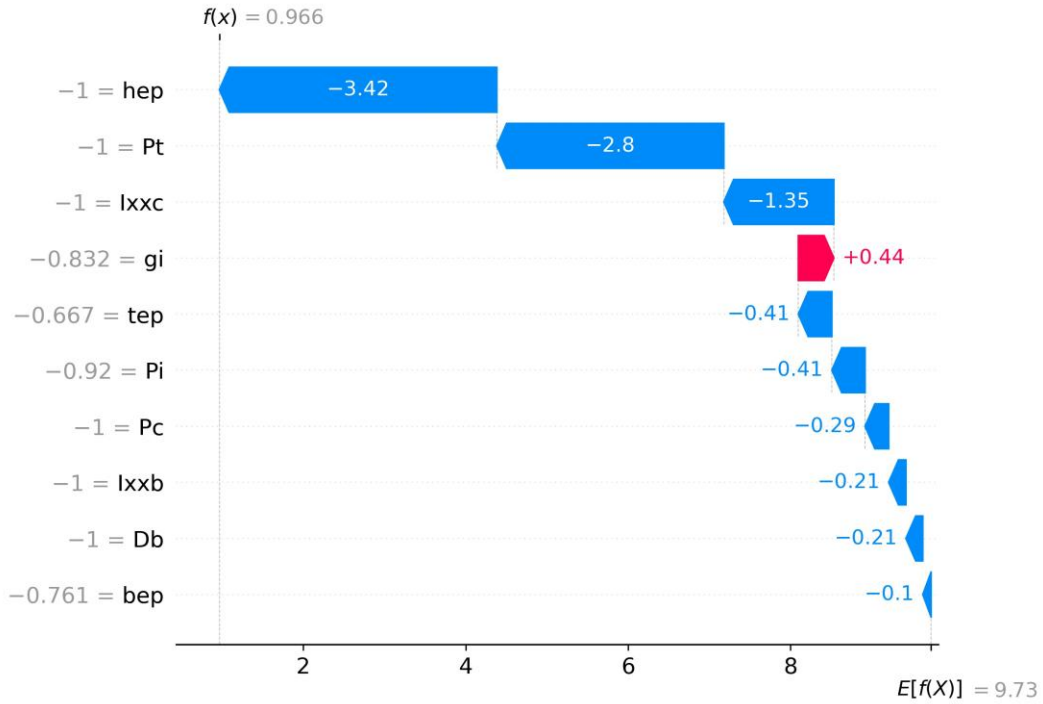
(a)



(b)



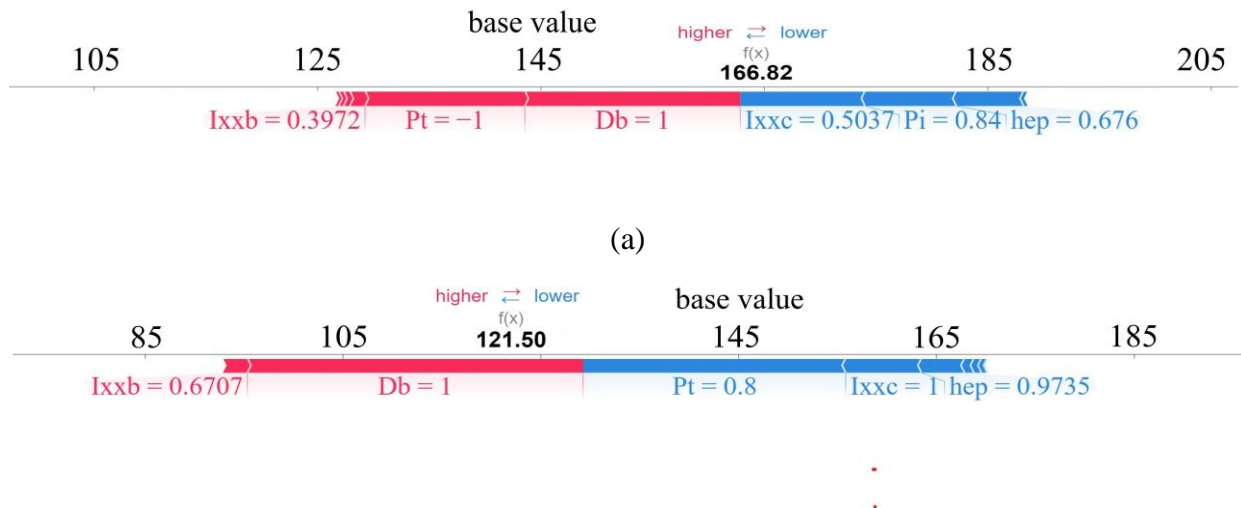
(c)



(d)

Fig. 14 SHAP waterfall plots for selected samples: (a) sample 10- (Actual value: 11.983 MN·m/rad); (b) sample 169- (Actual value: 5.01 MN·m/rad); (c) sample 253- (Actual value: 29.938 MN·m/rad); (d) sample 440- (Actual value: 0.987 MN·m/rad).

The base value and the output value in Fig. 15(a)–15(d), correspond to the average of the data set and the final prediction for a given observation. The difference between these two signals is the influence of the various features, which may have a positive or negative effect on the prediction. Thus, some features are red and increase the occurrence, while others are blue and reduce the level. For example, Fig. 15(a) presents evidence for a specific training data (sample 70), where the base value equals 145 m·rad, and the output value equals 166.82 m·rad, which are very close to the actual 165.23 m·rad. The example shows that the bolt size (D_b) and the spacing of the tension bolts (P_t) significantly increase the predicted ultimate rotation capacity. In contrast, the most significant feature, that adversely affects the result, is the second moment of inertia of the column (I_{xx}^c).



(a)

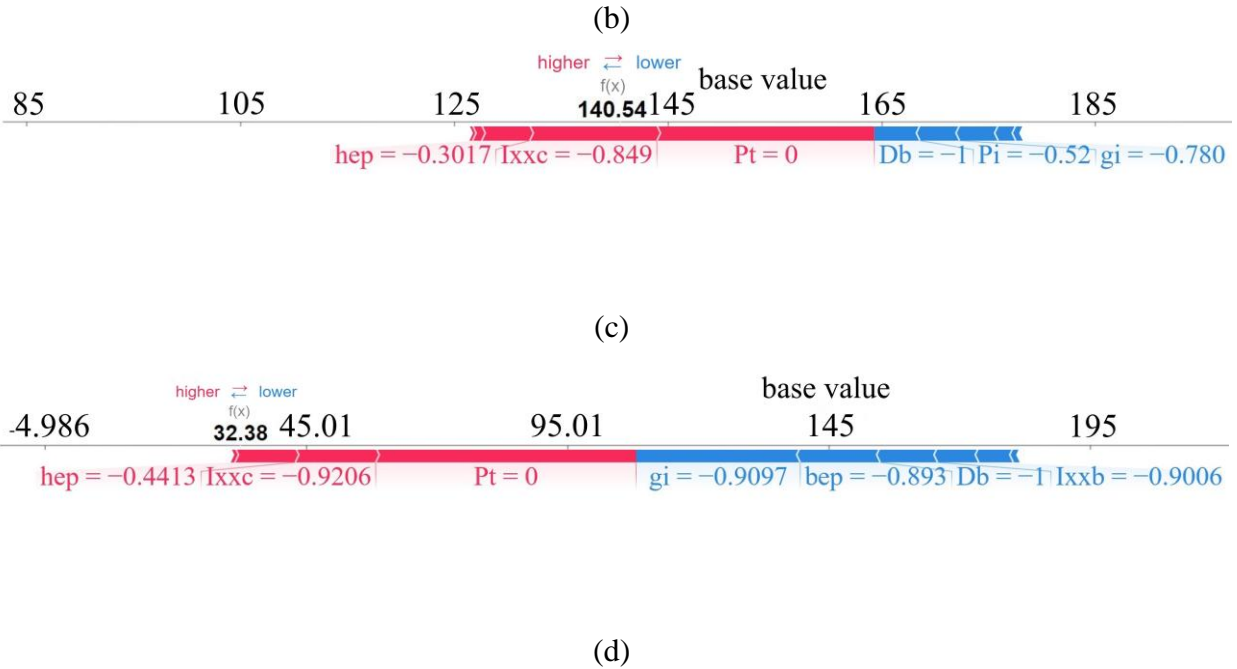


Fig. 15 SHAP individual force plots for selected samples: (a) sample 70- (Actual value: 165.23 m·rad); (b) sample 145- (Actual value: 123.13 m·rad); (c) sample 347- (Actual value: 142.73 m·rad); (d) sample 459- (Actual value: 33.10 m·rad).

In this section, SHAP was used to interpret the results from the ML models, selected based on their high performance in predicting target outcomes. Specifically, the XGBoost model was chosen for initial rotational stiffness ($S_{j,ini}$) and plastic moment resistance ($M_{j,R}$), while Gradient Boosting was used for maximum moment resistance ($M_{j,max}$) and ultimate rotation capacity ($\Phi_{j,u}$), as these models provided the most accurate predictions for these parameters. By focusing on SHAP's feature importance, it was possible to observe how individual geometrical and material properties affect connection behavior. For example, features like end-plate thickness (t_{ep}) had a positive SHAP value, suggesting a direct relationship with connection stiffness and strength, which aligns with prior findings. Similarly, a negative SHAP value for bolt spacing (P_t) indicated that larger bolt spacing could reduce rotational capacity, confirming the inverse relationship observed in our analysis. SHAP's outputs also allowed for straightforward comparison of feature impacts, for instance, t_{ep} consistently had higher SHAP values than other features, highlighting t_{ep} as a more influential factor in determining stiffness in the model's predictions. This approach supports the validity of the model's outputs and also allows structural designers to identify critical features that affect the moment rotation response of connections in stainless-steel designs.

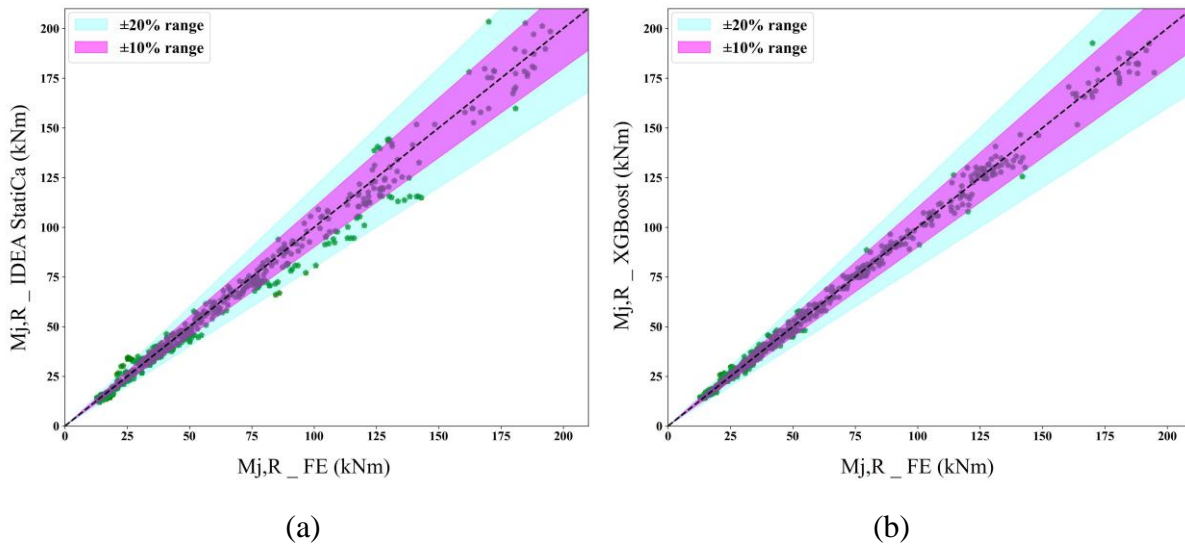
7 Comparing Machine Learning predictions of plastic moment resistance against recent proposed design calculation methods for stainless-steel joints

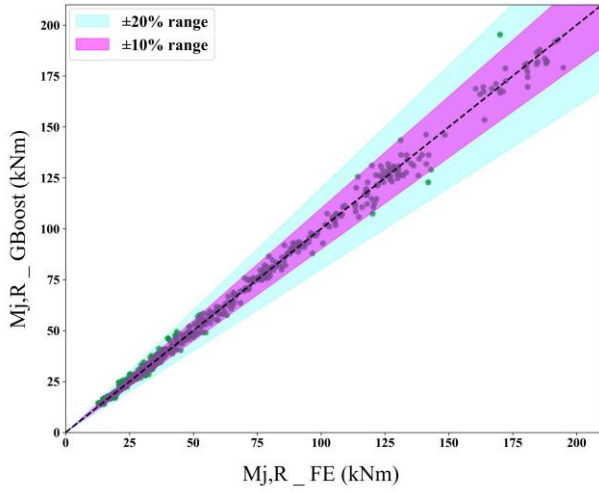
This section presents an examination of the design approach suggested by current authors [4,50] for determining plastic moment resistance, utilizing the IDEA StatiCa professional package [76]. The results are benchmarked against outcomes from FE models, as shown in Fig. 16(a). Figures 16(b)–16(i) provide a comparison between the earlier introduced predictive ML models for plastic moment resistance ($M_{j,R}$) and FE results.

It is worth noting that the yield stress, as a key parameter that determines the strength of materials, is generally defined in the case of carbon steel as the stress at an offset of 0.2% plastic strain, namely $f_{0.2}$. However, for stainless-steel, the 0.2% strain value, unlike with carbon steel, cannot determine the actual strength and ductility of the material. Stainless-steel maintains its quasi-linear behavior up to relatively significant stress states, with significant stiffness and strain hardening capability. Hence a novel method for

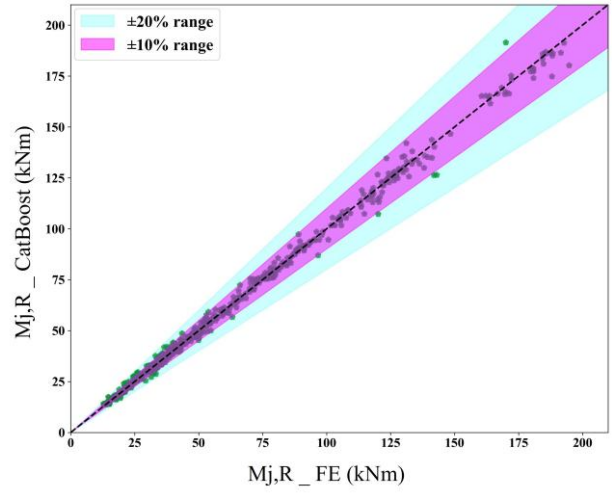
computing the plastic moment resistance of the material has been developed by current authors [50] to account for the significant strain-hardening effect of stainless-steel. This method is based on the post-elastic secant stiffness of stainless-steel and is used to provide input data to the IDEA StatiCa software for 612 FEP connections. The joints underwent analysis using the IDEA StatiCa connections software, which relies on the component-based finite element model (CBFEM). This method combines key features of the component method included in the Eurocode EN 1993-1-4 [49] with the computational power of FEM to design steel joints. Steel joints can be constructed incrementally using CBFEM. Subsequently, results conforming to the applicable code standards are generated. The structural joints can be constructed in IDEA StatiCa by implementing predefined manufacturing operations. The plates are connected solely by a weld component and are individually modeled. Bolts are modeled as springs with corresponding tensile and shear trilinear stiffness. An ideal elastic-plastic model that incorporates strain hardening and the true stress-strain diagram is employed to characterize the material. For regions not susceptible to buckling, the ultimate limit state criterion is set to 5%. For modeling the joint components, shell elements are employed, with four nodes in each corner, each with three translations and three rotations degrees of freedom. The shell is divided into five integration points along the plate thickness. There is a common size of element for all plates in a profile. A 10 mm minimum and 30 mm maximum element size is specified. Contacts between plates are modeled according to the “Penalty” method. The Multi-Point Constraint contact method is used for welding contact modeling, allowing elements with different meshing densities to be connected. According to the software manual [76], a theoretical length is defined for each connected member.

The comparison of plastic moment resistance derived from IDEA StatiCa against those from ABAQUS FE results, referenced in Fig. 16(a), is further expanded upon through eight additional graphs. These graphs contrast the plastic moment resistances predicted by various ML models (considering all data sets) against FE results depicted in Figs. 16(b)–16(i). Analysis of Fig. 16(a) indicates that the correlation between FE and CBFEM, using an equivalent material modeling approach, falls within an acceptable range regarding plastic moment resistance. The performance metrics achieved are $R^2 = 0.98$, $RMSE = 6.04$ kN·m, and $MAE = 3.87$ kN·m. This outcome affirms the effectiveness of the method proposed by the current researchers [50] for defining equivalent yield stress. Moreover, when examining the ML outcomes (Figs. 16(b)–16(i)), as depicted in detail in Table 4(b), XGBoost consistently outperforms all other models across the entire data set in terms of R^2 , MAE , and $RMSE$ scores, making it the top-performing model.

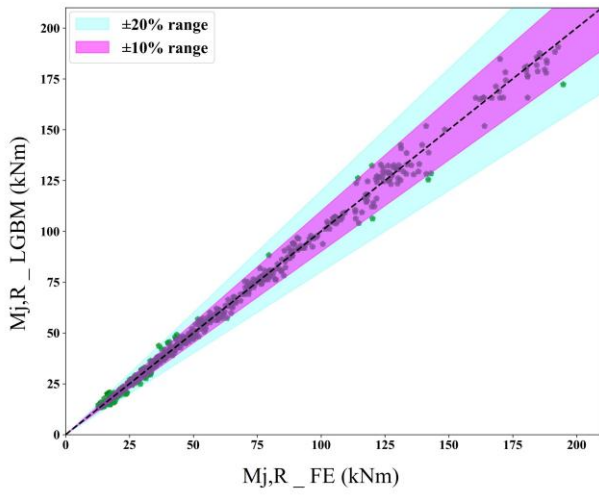




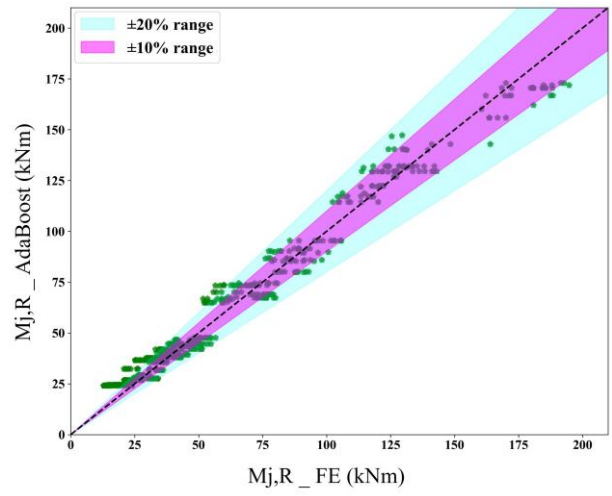
(c)



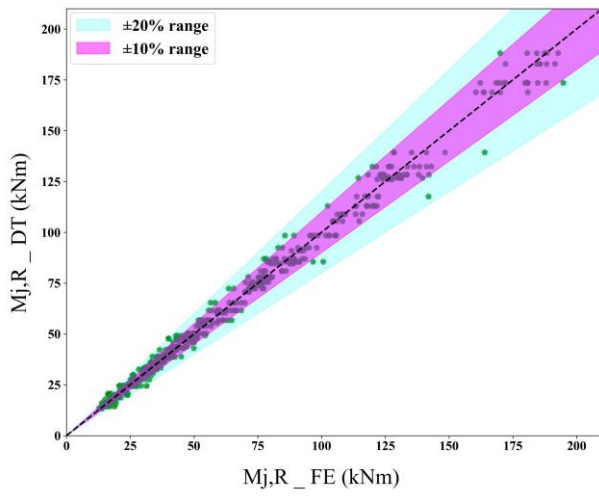
(d)



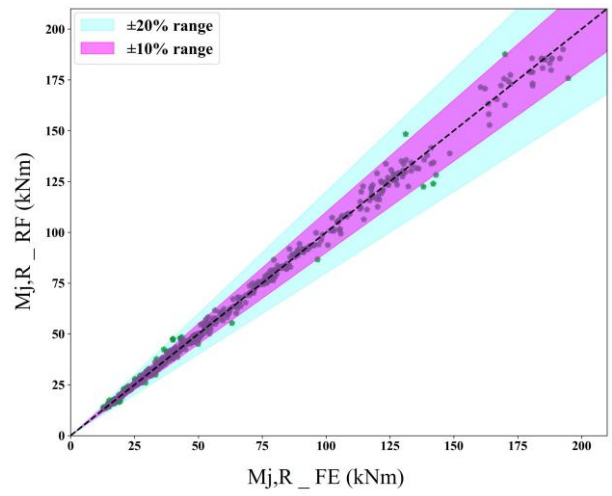
(e)



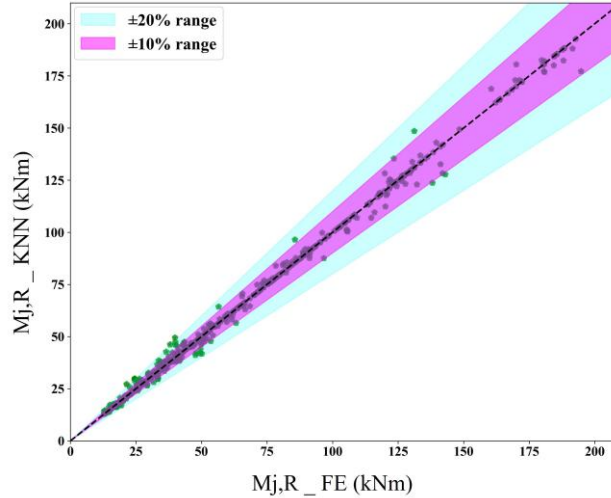
(f)



(g)



(h)



(i)

Fig. 16 Prediction of plastic moment resistance ($M_{j,R}$) for different models: (a) Prediction using IDEA StatiCa; (b) Prediction using XGBoost; (c) Prediction using Gradient Boosting (GBoost); (d) Prediction using CatBoost; (e) Prediction using LightGBM (LGBM); (f) Prediction using AdaBoost; (g) Prediction using Decision Tree (DT); (h) Prediction using Random Forest (RF); (i) Prediction using k-Nearest Neighbors (KNN).

8 Graphical user interface development

The results displayed above show that the proposed technique can predict the moment–rotation response of stainless-steel FECs with high accuracy. Therefore, the best performing ML models for output responses (XGBoost for $S_{j,ini}$ and $M_{j,R}$; GBoost for $M_{j,max}$, and $\Phi_{j,u}$) are implemented in the GUI application. To achieve this, tkinter [77], a python library, was utilized for GUI development, which links the user interface with the main software program, making use of object-oriented programming. The screenshot of this app (Fig. 17) illustrates the GUI tool, which is equipped with a wide range of capabilities that allow the users to analyze the performance of the connections fast and easy. Via the “Feature inputs” section on the top menu, users can enter the input features and a moment–rotation curve will be produced. The primary output results are found in the “Model output” menu bar, where the user gets to see the complete details of the connections. The GUI tool will also allow the user to change the parameter values and observe the effects of such values on the overall system response in real-time. The advantage of this feature is that it allows drawing multiple comparative curves by varying the value of a single parameter with other curves drawn previously being held constant. With this feature, users can easily fine-tune a connection to fit the demands of performance level. All the resources needed to install the GUI can be found at Ref. [78].

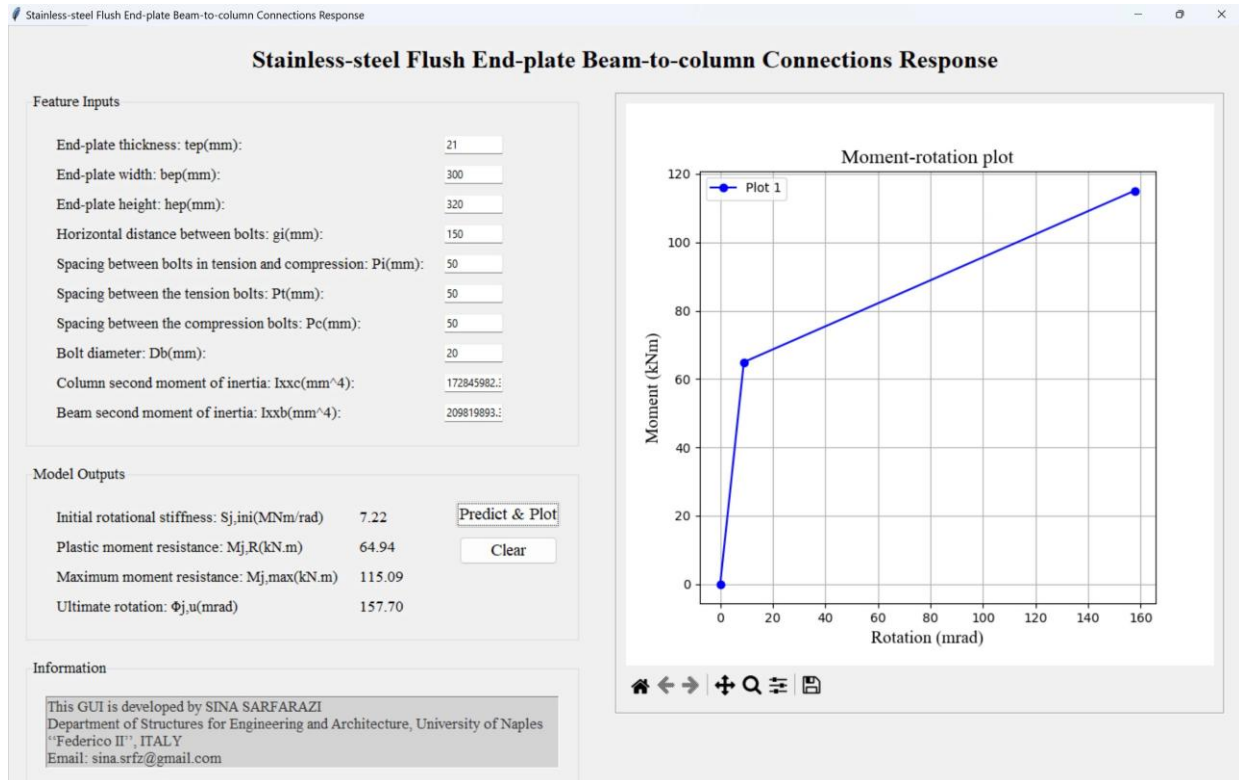


Fig. 17 Screenshot of the developed GUI.

9 Limitations and future work

Although the ML approach employed in this study has shown reliable predictive capabilities, some limitations should be pointed out. The data set used in this research mainly includes austenitic stainless-steel, as this type is utilized in structural applications and has a clear material modeling guideline available in EC3 Part 1-4 (EN 1993-1-4) [49]. Therefore, the results may not be fully applicable to other types of stainless-steel, such as ferritic or duplex, because they have different mechanical characteristics. Expanding the data set to include a wider variety of stainless-steel grades and configurations could enhance the model's adaptability to various structural uses. Another limitation is that the study focused on monotonic loading. Future research could include cyclic loading conditions to examine whether they alter the performance of stainless-steel connections and to potentially adjust the predictive models accordingly. Subsequent studies might expand the variety of geometric variations, like alternative cross-sectional shapes, and explore different connection types and configurations. Moreover, there is a necessity to examine the response of stainless-steel joints, especially those with two or four sides, focusing on scenarios where failure predominantly occurs in the column area. Additionally, integrating methods, such as Physics-Informed Neural Networks, could provide an expansion to the model by incorporating governing physical principles directly into the prediction process [79]. This approach would allow for the calculation of essential structural responses within the model itself, leading to improved accuracy and interpretability.

The integration of the developed GUI tool into existing engineering practices presents potential advantages and limitations. By providing rapid, data-driven predictions, this tool offers an efficient alternative to traditional methods, potentially streamlining workflows during preliminary design stages. However, broader validation of the tool in different structural contexts and configurations is necessary to ensure its accuracy and applicability across diverse engineering applications.

10 Conclusions

It is known that current design codes for stainless-steel connections were derived from carbon steel experimental and numerical studies, excluding the strain hardening and other specific characteristics of stainless-steel material. This may result in inaccurate and inefficient design and analyses of the stainless-steel beam to column connections. Therefore, there is a need to improve the current design methods to fully use stainless-steel's benefits. In this regard, this study presents a novel hybrid EML framework, which not only helps to improve understanding of the mechanical behavior of these connections but also provides a basis for further theoretical and practical developments in the investigated field.

The study can be resumed as follows.

1) A four-parameter curve fitting approach is presented. Then a comprehensive database of 612 samples is created, specifically focusing on FEP connections subjected to monotonic loading and fabricated from stainless-steel. To determine the geometry data range, special care is taken to incorporate all stainless-steel sections available from 5 different suppliers, following guidelines from the British Stainless-steel Association.

2) The developed database facilitated the execution of 32 ML analyses, including training, validation, and testing phases for four distinct target outputs. The predictive results were compared with those of FE analysis. For the initial rotational stiffness, XGBoost demonstrated the highest accuracy across the entire data set, based on R^2 , MAE , and $RMSE$ metrics. Regarding the plastic moment resistance, XGBoost performed best across the entire data set according to R^2 , MAE , and $RMSE$ scores. For ultimate rotation, GBoost led in performance on the entire data set based on R^2 metric, whereas KNN was the most accurate in terms of MAE and $RMSE$ metrics. Regarding the maximum moment resistance, GBoost performed best across the entire data set according to R^2 and $RMSE$ scores, while KNN excelled in the MAE metric.

3) Subsequently the most effective algorithms are applied in an explainable ML analysis using the SHAP algorithm. The SHAP values are not meant to define the cause-and-effect relationships between the model and the phenomenon they are explaining. Instead, their role is to give more information about how the model uses its inputs to produce the output. This demonstrates that the significant impact of an input feature on a model's prediction does not necessarily mean that the input feature is fundamentally important from a structural perspective regarding the behavior of the output. To solve the limitations that emerged from the black-box models, decision-makers should put a higher emphasis on explainable models to guarantee the accuracy of prediction and application. This will facilitate more informed decision-making processes. Structural design, commonly governed by codes and standards, is expected to potentially improve through the integration of data-driven models. These models could supplement or refine conventional design methodologies, particularly in areas inadequately addressed by existing regulations, such as the behavior of stainless-steel connections, which is the focus of the current study.

4) The final part of this research is the development of a GUI application based on trained machine-learning models that is applicable for estimating the moment–rotation curve of stainless-steel FEP connections.

By demonstrating its effectiveness with stainless-steel, the developed approach can influence future research and practical engineering and can provide a comprehensive framework for studying the behavior of beam-to-column connections, regardless of their type or material.

Conflicts of Interest The authors declare that they have no conflicts of interest.

References

1. Kong Z, Hong S, Vu Q V, Cao X, Kim S E, Yu B. New equations for predicting initial stiffness and ultimate moment of flush end-plate connections. *Journal of Constructional Steel Research*, 2020, 175: 106336 doi:10.1016/j.jcsr.2020.106336
2. Ciutina A, Nunes D L. Behavior of end-plate steel connections with 4 bolts per row under large deformations. In: Proceedings of the 9th International Conference on Steel and Aluminum Structures (ICSAS19). Bradford, UK: Independent Publishing Network; 2019. ISBN: 978-1-78972-197-3.
3. Zandonini R, Bursi O S. Monotonic and hysteretic behavior of bolted endplate beam-to-column joints. *Advances in Steel Structures (ICASS '02)*, 2002, 1: 81–94

4. Mascolo I, Guarracino F, Sarfarazi S, Della Corte G. A proposal for a simple characterization of stainless steel connections through an equivalent yield strength. *Structures*, 2024, 68: 107043 [doi:10.1016/j.istruc.2024.107043](https://doi.org/10.1016/j.istruc.2024.107043)
5. Shamass R, Guarracino F. Numerical and theoretical modeling of the web-post buckling of stainless-steel cellular beams. *ce/papers*, 2021, 4: 1551–1557
6. Afshan S, Gardner L. The continuous strength method for structural stainless-steel design. *Thin-walled Structures*, 2013, 68: 42–49 [doi:10.1016/j.tws.2013.02.011](https://doi.org/10.1016/j.tws.2013.02.011)
7. Kim T S, Kuwamura H. Finite element modeling of bolted connections in thin-walled stainless-steel plates under static shear. *Thin-walled Structures*, 2007, 45(4): 407–421 [doi:10.1016/j.tws.2007.03.006](https://doi.org/10.1016/j.tws.2007.03.006)
8. Bouchair A, Averseng J, Abidelah A. Analysis of the behavior of stainless-steel bolted connections. *Journal of Constructional Steel Research*, 2008, 64(11): 1264–1274 [doi:10.1016/j.jcsr.2008.07.009](https://doi.org/10.1016/j.jcsr.2008.07.009)
9. Salih E L, Gardner L, Nethercot D A. Bearing failure in stainless-steel bolted connections. *Engineering Structures*, 2011, 33(2): 549–562 [doi:10.1016/j.engstruct.2010.11.013](https://doi.org/10.1016/j.engstruct.2010.11.013)
10. Yuan H X, Hu S, Du X X, Yang L, Cheng X Y, Theofanous M. Experimental behavior of stainless-steel bolted T-stub connections under monotonic loading. *Journal of Constructional Steel Research*, 2019, 152: 213–224 [doi:10.1016/j.jcsr.2018.02.021](https://doi.org/10.1016/j.jcsr.2018.02.021)
11. Gao J D, Yuan H X, Du X X, Hu X B, Theofanous M. Structural behavior of stainless-steel double extended end-plate beam-to-column joints under monotonic loading. *Thin-walled Structures*, 2020, 151: 106743 [doi:10.1016/j.tws.2020.106743](https://doi.org/10.1016/j.tws.2020.106743)
12. Kong Z, Jin Y, Yang F, Vu Q V, Truong V, Yu B, Kim S E. Numerical simulation for structural behavior of stainless-steel web cleat connections. *Journal of Constructional Steel Research*, 2021, 183: 106706 [doi:10.1016/j.jcsr.2021.106706](https://doi.org/10.1016/j.jcsr.2021.106706)
13. Elflah M, Theofanous M, Dirar S, Yuan H X. Behavior of stainless-steel beam-to-column joints – Part I: Experimental investigation. *Journal of Constructional Steel Research*, 2019, 152: 183–193 [doi:10.1016/j.jcsr.2018.02.040](https://doi.org/10.1016/j.jcsr.2018.02.040)
14. Hasan M J, Al-Deen S, Ashraf M. Behavior of top seat double web angle connection produced from austenitic stainless-steel. *Journal of Constructional Steel Research*, 2019, 155: 460–479 [doi:10.1016/j.jcsr.2018.12.015](https://doi.org/10.1016/j.jcsr.2018.12.015)
15. Eladly M M, Schafer B W. Numerical and analytical study of stainless-steel beam-to-column extended end-plate connections. *Engineering Structures*, 2021, 240: 112392 [doi:10.1016/j.engstruct.2021.112392](https://doi.org/10.1016/j.engstruct.2021.112392)
16. Song Y, Li D, Uy B, Wang J. Ultimate behavior and rotation capacity of stainless-steel end-plate connections. *Steel and Composite Structures*, 2022, 42(4): 569–590
17. Žur K K, Firouzi N, Rabczuk T, Zhuang X. Large deformation of hyperelastic modified Timoshenko–Ehrenfest beams under different types of loads. *Computer Methods in Applied Mechanics and Engineering*, 2023, 416: 116368 [doi:10.1016/j.cma.2023.116368](https://doi.org/10.1016/j.cma.2023.116368)
18. Firouzi N, Alzaidi A S M, Nezaminia H, Dalalchi D. Numerical investigation on the effect of different parameters on nonlinear vibration response of fully geometrically exact Timoshenko beams. *Applied Physics. A, Materials Science & Processing*, 2024, 130(9): 618 [doi:10.1007/s00339-024-07775-2](https://doi.org/10.1007/s00339-024-07775-2)
19. Firouzi N, Alzaidi A S M. Non-linear elastic beam deformations with four-parameter Timoshenko beam element considering through-the-thickness stretch parameter and reduced integration. *Symmetry*, 2024, 16(8): 984 [doi:10.3390/sym16080984](https://doi.org/10.3390/sym16080984)
20. Samaniego E, Anitescu C, Goswami S, Nguyen-Thanh V M, Guo H, Hamdia K, Zhuang X, Rabczuk T. An energy approach to the solution of partial differential equations in computational mechanics via machine learning: Concepts, implementation and applications. *Computer Methods in Applied Mechanics and Engineering*, 2020, 362: 112790 [doi:10.1016/j.cma.2019.112790](https://doi.org/10.1016/j.cma.2019.112790)
21. Anitescu C, Atroshchenko E, Alajlan N, Rabczuk T. Artificial neural network methods for the solution of second-order boundary value problems. *Computers, Materials & Continua*, 2019, 59(1): 345–359 [doi:10.32604/cmc.2019.06641](https://doi.org/10.32604/cmc.2019.06641)
22. Liu B, Vu-Bac N, Rabczuk T. A stochastic multiscale method for the prediction of the thermal conductivity of polymer nanocomposites through hybrid machine learning algorithms. *Composite Structures*, 2021, 273: 114269 [doi:10.1016/j.compstruct.2021.114269](https://doi.org/10.1016/j.compstruct.2021.114269)
23. Liu B, Lu W, Olofsson T, Zhuang X, Rabczuk T. Stochastic interpretable machine learning based multiscale modeling in thermal conductivity of polymeric graphene-enhanced composites. *Composite Structures*, 2024, 327: 117601 [doi:10.1016/j.compstruct.2023.117601](https://doi.org/10.1016/j.compstruct.2023.117601)
24. Liu B, Vu-Bac N, Zhuang X, Fu X, Rabczuk T. Stochastic full-range multiscale modeling of thermal conductivity of polymeric carbon nanotubes composites: A machine learning approach. *Composite Structures*, 2022, 289: 115393 [doi:10.1016/j.compstruct.2022.115393](https://doi.org/10.1016/j.compstruct.2022.115393)
25. Liu B, Lu W. Surrogate models in machine learning for computational stochastic multi-scale modelling in composite materials design. *International Journal of Hydromechatronics*, 2022, 5(4): 336–365 [doi:10.1504/IJHM.2022.127037](https://doi.org/10.1504/IJHM.2022.127037)
26. Xia Y, Zhang C, Wang C, Liu H, Sang X, Liu R, Zhao P, An G, Fang H, Shi M, Li B, Yuan Y, Liu B. Prediction of bending strength of glass fiber reinforced methacrylate-based pipeline UV-CIPP rehabilitation materials based on machine learning. *Tunnelling and Underground Space Technology*, 2023, 140: 105319 [doi:10.1016/j.tust.2023.105319](https://doi.org/10.1016/j.tust.2023.105319)

27. Liu B, Vu-Bac N, Zhuang X, Fu X, Rabczuk T. Stochastic integrated machine learning based multiscale approach for the prediction of the thermal conductivity in carbon nanotube reinforced polymeric composites. *Composites Science and Technology*, 2022, 224: 109425 [doi:10.1016/j.compscitech.2022.109425](https://doi.org/10.1016/j.compscitech.2022.109425)
28. Liu B, Vu-Bac N, Zhuang X, Lu W, Fu X, Rabczuk T. Al-DeMat: A web-based expert system platform for computationally expensive models in materials design. *Advances in Engineering Software*, 2023, 176: 103398 [doi:10.1016/j.advengsoft.2022.103398](https://doi.org/10.1016/j.advengsoft.2022.103398)
29. Gao X, Lin C. Prediction model of the failure mode of beam-column joints using machine learning methods. *Engineering Failure Analysis*, 2021, 120: 105072 [doi:10.1016/j.engfailanal.2020.105072](https://doi.org/10.1016/j.engfailanal.2020.105072)
30. Mangalathu S, Jeon J. Classification of failure mode and prediction of shear strength for reinforced concrete beam-column joints using machine learning techniques. *Engineering Structures*, 2018, 160: 85–94 [doi:10.1016/j.engstruct.2018.01.008](https://doi.org/10.1016/j.engstruct.2018.01.008)
31. Alwanas A A H, Al-Musawi A A, Salih S Q, Tao H, Ali M, Yaseen Z M. Load-carrying capacity and mode failure simulation of beam-column joint connection: Application of self-tuning machine learning model. *Engineering Structures*, 2019, 194: 220–229 [doi:10.1016/j.engstruct.2019.05.048](https://doi.org/10.1016/j.engstruct.2019.05.048)
32. Park S H, Yoon D, Kim S, Geem Z W. Deep neural network applied to joint shear strength for exterior RC beam-column joints affected by cyclic loadings. *Structures*, 2021, 33: 1819–1832 [doi:10.1016/j.istruc.2021.05.031](https://doi.org/10.1016/j.istruc.2021.05.031)
33. Kotsoyova G M, Cotsovos D M, Lagaros N D. Assessment of RC exterior beam-column joints based on artificial neural networks and other methods. *Engineering Structures*, 2017, 144: 1–18 [doi:10.1016/j.engstruct.2017.04.048](https://doi.org/10.1016/j.engstruct.2017.04.048)
34. Haido J H. Prediction of the shear strength of RC beam-column joints using new ANN formulations. *Structures*, 2022, 38: 1191–1209 [doi:10.1016/j.istruc.2022.02.046](https://doi.org/10.1016/j.istruc.2022.02.046)
35. Alagundi S, Palanisamy T. Neural network prediction of joint shear strength of exterior beam-column joint. *Structures*, 2022, 37: 1002–1018 [doi:10.1016/j.istruc.2022.01.013](https://doi.org/10.1016/j.istruc.2022.01.013)
36. Naderpour H, Nagai K. Shear strength estimation of reinforced concrete beam-column sub-assemblages using multiple soft computing techniques. *Structural Design of Tall and Special Buildings*, 2020, 29(9): e1730 [doi:10.1002/tal.1730](https://doi.org/10.1002/tal.1730)
37. Shah S N R, Ramli Sulong N H, El-Shafie A. New approach for developing soft computational prediction models for moment and rotation of boltless steel connections. *Thin-walled Structures*, 2018, 133: 206–215 [doi:10.1016/j.tws.2018.09.032](https://doi.org/10.1016/j.tws.2018.09.032)
38. Cao Y, Wakil K, Alyousef R, Jermstiparsert K, Si Ho L, Alabduljabbar H, Alaskar A, Alrshoudi F, Mustafa Mohamed A. Application of extreme learning machine in behavior of beam to column connections. *Structures*, 2020, 25: 861–867 [doi:10.1016/j.istruc.2020.03.058](https://doi.org/10.1016/j.istruc.2020.03.058)
39. Abdalla K M, Stavroulakis G E. A backpropagation neural network model for semi-rigid steel connections. *Computer-Aided Civil and Infrastructure Engineering*, 1995, 10(2): 77–87 [doi:10.1111/j.1467-8667.1995.tb00271.x](https://doi.org/10.1111/j.1467-8667.1995.tb00271.x)
40. Faridmehr I, Nikoo M, Pucinotti R, Bedon C. Application of component-based mechanical models and artificial intelligence to bolted beam-to-column connections. *Applied Sciences (Basel, Switzerland)*, 2021, 11(5): 2297 [doi:10.3390/app11052297](https://doi.org/10.3390/app11052297)
41. Kueh C Y. Artificial neural network and regressed beam-column connection explicit mathematical moment-rotation expressions. *Journal of Building Engineering*, 2021, 43: 103195 [doi:10.1016/j.jobe.2021.103195](https://doi.org/10.1016/j.jobe.2021.103195)
42. Zakir Sarothi S, Sakil Ahmed K, Imtiaz Khan N, Ahmed A, Nehdi M L. Predicting bearing capacity of double shear bolted connections using machine learning. *Engineering Structures*, 2022, 251: 113497 [doi:10.1016/j.engstruct.2021.113497](https://doi.org/10.1016/j.engstruct.2021.113497)
43. Anderson D, Hines E L, Arthur S J, Eiap E L. Application of artificial neural networks to the prediction of minor axis steel connections. *Computers & Structures*, 1997, 63(4): 685–692 [doi:10.1016/S0045-7949\(96\)00080-6](https://doi.org/10.1016/S0045-7949(96)00080-6)
44. Tran V L, Kim J K. Revealing the nonlinear behavior of steel flush endplate connections using ANN-based hybrid models. *Journal of Building Engineering*, 2022, 57: 104878 [doi:10.1016/j.jobe.2022.104878](https://doi.org/10.1016/j.jobe.2022.104878)
45. de Lima L R O, Vellasco P C G D S, de Andrade S A L, da Silva J G S, Vellasco M M B R. Neural networks assessment of beam-to-column joints. *Journal of the Brazilian Society of Mechanical Sciences and Engineering*, 2005, 27(3): 314–324 [doi:10.1590/S1678-58782005000300015](https://doi.org/10.1590/S1678-58782005000300015)
46. British Stainless-Steel Association. BSSA stainless-steel sections directory. 2nd ed. UK: British Stainless-Steel Association, 2006 https://bssa.org.uk/bssa_articles/bssa-stainless-steel-sections-directory-all-parts/
47. ABAQUS Incorporated. ABAQUS analysis user's manual for version 6.12, 2012
48. Sarfarazi S, Shamass R, Della Corte G, Guarracino F. Assessment of design approaches for stainless-steel joints through an equivalent FE modelling technique. *ce/papers*, 2022, 5(4): 271–281
49. EN 1993-1-4:2006. Eurocode 3: Design of Steel Structures—Part 1-4: General Rules—Supplementary Rules for Stainless Steels. Brussels: European Committee for Standardization, 2006
50. Sarfarazi S, Shamass R, Mascolo I, Della Corte G, Guarracino F. Some considerations on the behavior of bolted stainless-steel beam-to-column connections: A simplified analytical approach. *Metals*, 2023, 13(4): 753 [doi:10.3390/met13040753](https://doi.org/10.3390/met13040753)

51. Rasmussen K J. Full range stress-strain curves for stainless-steel alloys. *Journal of Constructional Steel Research*, 2003, 59(1): 47–61 [doi:10.1016/S0143-974X\(02\)00018-4](https://doi.org/10.1016/S0143-974X(02)00018-4)
52. Breda A, Coppeters S, Kuwabara T, Debruyne D. The effect of plastic anisotropy on the calibration of an equivalent model for clinched connections. *Thin-walled Structures*, 2019, 145: 106360 [doi:10.1016/j.tws.2019.106360](https://doi.org/10.1016/j.tws.2019.106360)
53. Sarfarazi S, Saffari H, Fakhreddini A. Shear behavior of panel zone considering axial force for flanged cruciform columns. *Civil Engineering Infrastructures Journal*, 2020, 53(2): 359–377
54. Saffari H, Sarfarazi S, Fakhreddini A. A mathematical steel panel zone model for flanged cruciform columns. *Steel and Composite Structures*, 2016, 20(4): 851–867 [doi:10.12989/scs.2016.20.4.851](https://doi.org/10.12989/scs.2016.20.4.851)
55. Sarfarazi S, Fakhreddini A, Modaresahmadi K. Evaluation of panel zone shear strength in cruciform columns, box-columns and double-web columns. *International Journal of Structural and Civil Engineering Research*, 2016, 5(1): 52–56 [doi:10.18178/ijscer.5.1.52-56](https://doi.org/10.18178/ijscer.5.1.52-56)
56. Shi Y, Shi G, Wang Y. Experimental and theoretical analysis of the moment–rotation behavior of stiffened extended end-plate connections. *Journal of Constructional Steel Research*, 2007, 63(9): 1279–1293 [doi:10.1016/j.jcsr.2006.11.008](https://doi.org/10.1016/j.jcsr.2006.11.008)
57. Pedregosa F, Varoquaux G, Gramfort A, Michel V, Thirion B, Grisel O, Blondel M, Prettenhofer P, Weiss R, Dubourg V, et al. Scikit-learn: Machine learning in Python. *Journal of Machine Learning Research*, 2011, 12: 2825–2830
58. Thai H T. Machine learning for structural engineering: A state-of-the-art review. *Structures*, 2022, 38: 448–491 [doi:10.1016/j.istruc.2022.02.003](https://doi.org/10.1016/j.istruc.2022.02.003)
59. Breiman L. Random forests. *Machine Learning*, 2001, 45(1): 5–32 [doi:10.1023/A:1010933404324](https://doi.org/10.1023/A:1010933404324)
60. Peterson L E. K-nearest neighbor. *Scholarpedia*, 2009, 4(2): 1883 [doi:10.4249/scholarpedia.1883](https://doi.org/10.4249/scholarpedia.1883)
61. Le Q H, Nguyen D H, Sang-To T, Khatir S, Le-Minh H, Gandomi A H, Cuong-Le T. Machine learning-based models for predicting compressive strength of geopolymers. *Frontiers of Structural and Civil Engineering*, 2024, 18(7): 1028–1049 [doi:10.1007/s11709-024-1039-5](https://doi.org/10.1007/s11709-024-1039-5)
62. Friedman J H. Greedy function approximation: A gradient boosting machine. *Annals of Statistics*, 2001, 29(5): 1189–1232 [doi:10.1214/aos/1013203451](https://doi.org/10.1214/aos/1013203451)
63. Chen T, Guestrin C. XGBoost: A scalable tree boosting system. In: *Proceedings of the 22nd ACM SIGKDD International Conference on Knowledge Discovery and Data Mining*. New York: Association for Computing Machinery, 2016, 785–794
64. Chen S, Chen C, Li S, Guo J, Guo Q, Li C. Predicting torsional capacity of reinforced concrete members by data-driven machine learning models. *Frontiers of Structural and Civil Engineering*, 2024, 18(4): 444–460 [doi:10.1007/s11709-024-1050-x](https://doi.org/10.1007/s11709-024-1050-x)
65. Ke G, Meng Q, Finley T, Wang T, Chen W, Ma W, Ye Q, Liu T Y. LightGBM: A highly efficient gradient boosting decision tree. In: *Proceedings of the 31st International Conference on Neural Information Processing Systems*. New York: Curran Associates Incorporated, 2017, 3149–3157
66. Qiong T, Jha I, Bahrami A, Isleem H F, Kumar R, Samui P. Proposed numerical and machine learning models for fiber-reinforced polymer concrete-steel hollow and solid elliptical columns. *Frontiers of Structural and Civil Engineering*, 2024, 18(7): 1169–1194 [doi:10.1007/s11709-024-1083-1](https://doi.org/10.1007/s11709-024-1083-1)
67. Freund Y, Schapire R E. A decision-theoretic generalization of on-line learning and an application to boosting. *Journal of Computer and System Sciences*, 1997, 55(1): 119–139 [doi:10.1006/jcss.1997.1504](https://doi.org/10.1006/jcss.1997.1504)
68. Freund Y, Schapire R E. Experiments with a new boosting algorithm. In: *Proceedings of the 13th International Conference on Machine Learning*. San Francisco: Morgan Kaufmann Publishers Incorporated, 1996, 148–156
69. Ferreira A J, Figueiredo M A T. Boosting Algorithms: A Review of Methods, Theory, and Applications. In: *Ensemble Machine Learning: Methods and Applications*. New York: Springer, 2012, 35–85
70. Abarkan I, Rabi M, Ferreira F P V, Shamass R, Limbachiya V, Jweihan Y S, Pinho Santos L F. Machine learning for optimal design of circular hollow section stainless-steel stub columns: A comparative analysis with Eurocode 3 predictions. *Engineering Applications of Artificial Intelligence*, 2024, 132: 107952 [doi:10.1016/j.engappai.2024.107952](https://doi.org/10.1016/j.engappai.2024.107952)
71. Lundberg S M, Lee S I. A unified approach to interpreting model predictions. In: *Proceedings of the 31st International Conference on Neural Information Processing Systems*. New York: Curran Associates Incorporated, 2017, 4768–4777
72. Lai D, Demartino C, Xiao Y. Interpretable machine-learning models for maximum displacements of RC beams under impact loading predictions. *Engineering Structures*, 2023, 281: 115723 [doi:10.1016/j.engstruct.2023.115723](https://doi.org/10.1016/j.engstruct.2023.115723)
73. Karathanasopoulos N, Singh A, Hadjidoukas P. Machine learning-based modelling, feature importance and Shapley additive explanations analysis of variable-stiffness composite beam structures. *Structures*, 2024, 62: 106206 [doi:10.1016/j.istruc.2024.106206](https://doi.org/10.1016/j.istruc.2024.106206)
74. Wang S, Liu J, Wang Q, Dai R, Chen K. Prediction of non-uniform shrinkage of steel-concrete composite slabs based on explainable ensemble machine learning model. *Journal of Building Engineering*, 2024, 88: 109002 [doi:10.1016/j.jobee.2024.109002](https://doi.org/10.1016/j.jobee.2024.109002)

75. Liu T, Cakiroglu C, Islam K, Wang Z, Nehdi M L. Explainable machine learning model for predicting punching shear strength of FRC flat slabs. *Engineering Structures*, 2024, 301: 117276 [doi:10.1016/j.engstruct.2023.117276](https://doi.org/10.1016/j.engstruct.2023.117276)
76. IDEA StatiCa. IDEA StatiCa: User Guide, 2018 Available at: <https://www.ideastatica.com/connection-design>
77. Lundh F. An Introduction to Tkinter. 1999 (available at the website of Pythonware)
78. Sarfarazi S. Stainless-steel Flush End-plate Beam-to-Column Connections Response GUI. 2024 (available at the website of [GitHub](#))
79. Liu B, Wang Y, Rabczuk T, Olofsson T, Lu W. Multi-scale modeling in thermal conductivity of polyurethane incorporated with phase change materials using physics-informed neural networks. *Renewable Energy*, 2024, 220: 119565 [doi:10.1016/j.renene.2023.119565](https://doi.org/10.1016/j.renene.2023.119565)